UNIVERSIDAD DE CHILE
FACULTAD DE CIENCIAS FÍSICAS Y MATEMÁTICAS
DEPARTAMENTO DE INGENIERÍA ELÉTRICA

COTS BASED MAGNETO-RESISTIVE MAGNETOMETER FOR 3U CUBSAT PLATFORM AND MAGNETOSPHERIC IN SITU MEASUREMENTS

TESIS PARA OPTAR AL GRADO DE MAGÍSTER EN CIENCIAS DE LA INGENIERÍA, MENCIÓN ELÉCTRICA

MEMORIA PARA OPTAR AL TÍTULO DE INGENIERO CIVIL ELECTRICO

JOAQUÍN MATEO DÍAZ PEÑA

PROFESOR GUÍA:
MARCOS ÁNDRES DÍAZ QUEZADA

MIEMBROS DE LA COMISIÓN:
ÁNGEL CHRISTIAN ABUSLEME HOFFMAN
NICOLÁS ANDRÉS REYES GUZMAN

Este trabajo ha sido parcialmente financiado por
CONICYTPCHA/MagísterNacional/2015-22150792
y por el Departamento de Postgrado y Postítulo de la Universidad de Chile

SANTIAGO DE CHILE
2017

RESUMEN DE LA TESIS/MEMORIA PARA OPTAR AL
TÍTULO DE Ingeniero Civil Electrico y al grado de
Magíster en Ciencias de la Ingeniería, Mención Eléctrica
POR: Joaquín Mateo Díaz Peña
FECHA: 2017
PROF. GUÍA: DR. Marcos Ándres Díaz Quezada

COTS BASED MAGNETO-RESISTIVE MAGNETOMETER FOR 3U CUBSAT PLATFORM AND MAGNETOSPHERIC IN SITU MEASUREMENTS

Los sensores magnéticos son ampliamente utilizados siendo de gran ayuda en la navegación al ser usados como como una brújula, memorias magnéticas para ordenadores, sistemas automáticos, control de automóviles y detección. Incluso han sido determinantes en medicina mediante la medición del campo magnético del corazón, cerebro o pulmones, revelando información importante acerca de las corrientes dentro del cuerpo. Estas aplicaciones son ampliamente revisadas en la literatura actual, pero la importancia radica en que tienen el mismo centro: el magnetómetro.

En el presente trabajo, un magnetómetro es parte de una misión de investigación que se desplegarán en la misión CubeSat SUCHAI 2 y 3 para mediciones in-situ de campo magnético en la magnetosfera bajo el nombre de MAG-SPEL (Magnetometer of Space and Planetary Exploration Laboratory). Este tipo de medición se realiza principalmente por medio de los magnetómetros de gama alta, tales como Search Coil o Flux Gate, que son grandes y robustos. La presente tesis tendrá un enfoque diferente: pequeña escala y sensores de poco valor para los satélites pequeños (CubeSat) solamente usando COTS (componentes comprables de manera fácil y rápida), siguiendo el trabajo realizado por Imperial College y su sensor MAGIC.

En este caso los sensores son: pequeños, baratos, replicables, medianamente sensibles y de consumo moderado. Para esto se diseñó todo el sistema mediante el uso de un sensor comercial (HMC1001) y un front-end electrónico acorde para procesar la señal, utilizando las guías del magnetómetro MAGIC con la perspectiva de lograr mejoras tales como: diseño modular, cambio de rieles de voltaje, mejoras sobre el espectro de ruido y tratamiento de la señal differencial, culminando en una mejora de la sensitividad.

Se realizaron pruebas para cuantificar las variables de interés, tales como corriente de polarización y consumo, para luego pasar a realizar una calibración utilizando una Helmholzt Cage y un magnetómetro de referencia para una calibración cruzada. Esta calibración se realizó en Boston University utilizando equipo especializado para tal calibración. Todo esto con el fin de demostrar que se puede lograr generar un sensor magnético competitivo basado en MAGIC.

Finalmente se logró obtener un magnetómetro levemente superior en comparación al realizado por Imperial College, logrando una sensitividad de 10 – 50 nT cumpliendo todas las mejoras prometidas alcanzando rangos dinámicos de 45.000 nT y consumos alrededor de 1 W en funcionamiento tri axial además de cumplir con las restricciones impuestas por una misión CubeSat

Dedicated to an 18 year old Joaquín,
who wanted to be a scientist,
but thought he never could

Agradecimientos

Quiero partir agradeciendo a todos aquellos que estuvieron ahí para apoyarme. A los que me impulsaron a no dejar mis sueños de lado y a siempre seguir, siempre intentar y siempre perseverar en mis objetivos. Quiero agradecer a mi familia: a mi mamá Mónica por el apoyo incondicional y por habérsela jugado hasta las últimas, por siempre estar ahí en los momentos difíciles, por ser un ejemplo a seguir y un referente sobre lo que deseo ser. A Martín y Natalia, mis hermanos, que sin ellos no podría estar donde estoy, les agradezco la paciencia, el cariño y las incesantes bromas. También quiero agradecerá mis amigos, Tania, Su Rubiosidad Cristian, Gianni, Choripe y a todos en Pumón y Simba por el apoyo constante, por hacerse el tiempo para escucharme, para ayudarme a reírme de todo lo que esté pasando y por enseñarme a ser yo mismo. Sin ustedes esta tesis hubiera sido terminada seis meses antes. Debo agradecer de la misma forma a Gerardo, Caro y a todos los OPAMPs, por ayudarme a sobrevivir esta dura carrera sin perder la cordura, por enseñarme a aceptar mi ñoñes y estar orgulloso de ella.

Quiero agradecer a Marcos por ser mi mentor, por enseñarme que "fallar es parte del proceso" y que nunca hay que darse por vencido, que hay que creer en sus propios resultados y reírse de uno mismo es vital. Gracias por ser un excelente profesor guía y amigo, por soportarme y por ayudarme a lograr todos mis objetivos, por estar ahí durante toda mi carrera como investigador en SPEL. Quiero agradecer a Ángel por ayudarme en los momentos de duda vocacional, por prestarme espacio en su oficina para trabajar, por sus consejos y por su disposición. Te debo muchas cosas, mis inicios como investigador comenzaron contigo. Debo agradecer a Miguel "el guru" Patiño, por sus ideas, sus desayunos en su oficina, y por ser de gran ayuda durante todo el proceso, siempre agregando y preguntando lo preciso. Le agradezco a toda la gente de SPEL por el apoyo moral y técnico que me dieron durante el desarrollo de mi tesis, es un agrado trabajar con ustedes y nunca faltaron los momentos de ocio y risa. También le agradezco a Milena, por ayudarme en todo e ir más allá de lo que si trabajo le pedía, además de ser una amiga y confidente. Muchas gracias también a toda la gente de BU que me recibió, a Josh, Brian y todos los investigadores tanto del quinto como del séptimo piso. Por recibirme con los brazos abiertos, ayudarme en mi investigación y convencerme que estudiar allá es la mejor decisión que he tomado.

Muchas gracias a Conicyt, que a través de su programa de Becas Conicyt financió mi magister (CONICYTPCHA/MagísterNacional/2015-22150792), además del programa de Fondecyt (Fondecyt 1151476 A, y Fondecyt 1161356). También quiero agradecer al Departamento de Postgrado y Postítulo de la Universidad de Chile por su financiamiento.

Acknowledgements

I want to start thanking all those who were there to support me. To those who urged me not to leave my dreams aside and to always follow them, always try and always persevere in my goals. I want to thank my family: my mother Mónica for the unconditional support and for going with it to the last, for always being there in the difficult moments, for being an example to follow and a referent for me. To Martin and Natalia, my siblings, who without them, I could not be where I am, thank you for the patience, the affection and the incessant jokes. I also want to thank my friends, Tania, Su Rubiosidad Cristian, Gianni, Choripe and everyone in Pumón y Simba for the constant support, for making time to listen to me, to help me laugh at everything that is happening and for teaching me to be myself. Without you this thesis would have been completed six months earlier. I must also thank Gerardo, Caro and all the OPAMPs for helping me to survive this tough career without losing my sanity, for teaching me to accept my nerdiness and be proud of it.

I want to thank Marcos for being my mentor, for teaching me that "failing is part of the process" and that you can never give up, that you have to believe in your own results and laughing about oneself is vital. Thank you for being an excellent advisor and friend, for supporting me and for helping me achieve all my goals, for being there throughout my career as a SPEL researcher. I want to thank Angel, for helping me during moments of vocational doubt, for giving me space in his office to work, for his advice and for his disposition. I owe you many things, my beginnings as a researcher began with you. I must thank Miguel "the guru" Patiño, for his ideas, the breakfasts in his office, and for being a great help throughout the process, always adding and asking what was precise for the moment. I would like to thank everyone at SPEL for the moral and technical support they gave me during the development of my thesis, it is a pleasure to work with you and there were always moments for leisure and laughter. I also want to thank Milena, for helping me in everything and going beyond what her job asks for, as well as being a friend and confidant. Many thanks to everyone at BU who received me, Josh, Brian and all the researchers on both the fifth and seventh floors. For the welcome with open arms, for the help in my research, and for convincing me that studying there is the best decision I have ever made.

Many thanks to Conicyt, who through their Becas Nacionales program financed my magister (CONICYTPCHA/MagísterNacional/2015-22150792), in addition to the Fondecyt program (Fondecyt 1151476 and Fondecyt 1161356). I also want to thank the Postgraduate Department of the University of Chile for its funding.

Contents

List of Tables

List of Figures

Chapter 1

Introduction

1.1 Motivation and background

The irruption of a miniaturized satellite standard, the Cubesat, has propelled the development of new space missions at an affordable cost. Since its conception in 1999, many Cubesats have been launched into space. The scientific potentialities of this standard have been already recognized and discussed. The standard is offering unprecedented opportunities to groups and/or institutions in developing countries without much history/experience in satellite technology [5]. This is the case of the space program at the University of Chile [6]. The Satellite of the University of Chile (SUCHAI-1) is the first Cubesat built in Chile. This pico-satellite, 1U (10 cm x 10 cm 10 cm) Cubesat, is currently waiting for launch in Sharikahur, India. The Universidad de Chile space program is moving forward to the next mission, which includes 2 new Cubesats (SUCHAI-2 and SUCHAI-3). This time these Cubestas are 3U (10 cm x 10 cm x 30 cm), which falls in the nano-satellite category. The SUCHAI-2 and -3 are design for space research, in particular for magnetospheric and ionospheric measurements [6]. The magnetic field will be measured by using a deployable Anisotropic Magneto Resistance (AMR) magnetometer.

Magnetic fields are essential in characterizing different plasma regions in and around the Earth magnetosphere. Fluxgate magnetometers, such as those in the NASA led THEMIS mission [7] and similar to those used in the magnetometer array SAMBA, are the most common sensors to probe Earth's magnetic field in space [8] [9]. The fluxgates, using the ring core geometry multiple axis measurements can be achieved with extreme simplicity, controlling frequency and feedback field [10]. Missions like the Pioneer 11 [11], BepiColombo [12] and DAWN [13] have considered fluxgate magnetometer. This is not something strange considering that commercial fluxgate does exist [14]. COTS versions of the type of magnetometer exist and are the ones with a larger commercial history [9] [14]. However, heritage fluxgates sensor designs are not optimized for deployment on ultra-small satellites, such as Cubesats. The magnetoresitance (MR) magnetometers have more appropriate mass, volume and cost for nano-satellite missions, especially considering that the sensor has to be deployed long out of the satellite to avoid magnetic interference from the internal electronics and thus to provide a more accurate measurement. There are many types of magnetoresitance (MR)

magnetometers, such as the Giant, Tunneling and Anisotropic MR [15]. However, AMR magnetometer has the best features to be used as a space-borne magnetometer [16]. The AMR magnetometer intrinsic performance is not sufficient for many space science applications. Nevertheless, [17] suggest that operating the sensor in a driven, first-order closed loop mode, significantly improves low field sensitivity and offset drift. The magnetometer suggested by [17] is inexpensive, simple to implement and sensitive enough for scientific applications including detection of geomagnetic waves and structures. In particular, periodic cycle 5 (PC-5) magnetic oscillations at polar regions (aurora oval) have proven to be measurable with the improved features of AMR magnetometers [brow14 and DICE]. A three-axis design of AMR is currently used in the TRIO-CINEMA Cubesat constellation mission [17] and was also used in DICE mission [18]. The coming missions at University of Chile (two 3U Cubesats) will include AMR magnetometers in similar topology to that developed in the Magnetometer of Imperial College (MAGIC) [17][16], which is currently used in the TRIO-CINEMA mission. The system uses a COTS AMR magnetometer provided by Honeywell, HMC1001.

Although MAGIC [17] [16] is an important advancement to have an operational magnetic sensor for space science applications, it suffers of some drawbacks. First, MAGIC operates in a partial open loop configuration and therefore it exhibits worst offset drift than a fully closed loop implementation. The offset drift can be solved with on-board temperature calibrations but other issues of having a partial open loop configuration, such as the restrictions in the dynamic range of the sensor, cannot be solved by calibrations. Second, the op-amps selection can be improved. The electronic components are unable to provide the current needed by the HMC1001 for the nulling process of the magnetic field inside the device. On the other hand the electronic topology of MAGIC is not fully differential, which degrades the demodulation process due to resistances mismatches increasing the noise of the measurements. Finally, the current pulses generation stage requires a 17V power supply, which is not commonly included in Cubesat power systems.

1.2 Hypotheses

The Cubesat standard imposes serious constrains due to the small volume and weight. Thus, the sensors that Cubesats can carry within them needs to be: light in weight, small in size, of low power consumption and, ideally, of low cost.

As such, the current thesis hypotheses is: it is possible to use different topologies and components in order to improve the performance of the previous circuit presented by MAGIC, and thus the sensor itself.

1.3 Objective and methodology

The main objective is to build and test a functional magnetometer, improving circuits that are already widely used and to be a startup point for a future magnetometer array. The advantage of working on an already tested sensor is that there is some flight experience for

the components and knowledge for further inquiry.

To prove that it is possible to build a magnetic sensor based on the one built by Imperial College version MAGIC with improved sensitivity, the design must consider the different restrictions that the SUCHAI missions has, such as power and space. This translates into a sensor that should accomplish the following:

- Large dynamic range for earth like magnetic field measurements and larger than ±30.000 nT.
- Small sensitivity to achieve a reasonable measurement, meaning less than 40 nT of sensitivity.
- Current management that not exceeds the 4 A available in a CubeSat.

This work will analysis different circuits and possibilities of improvements of the current circuit, so to be able of generating a new sensor or add new capabilities to the already functional one.

1.3.1 Methodology

The methodology will be based on the proper steps to build any normal circuit, such as simulations, prototypes and general reviews. The steps of such work will be:

1. Study of the current state of the art of magnetic sensor
2. Simulation block by block for the proper understanding of the circuit, due to the magnetic phenomena and possible hysteresis some abstractions will have to be made.
3. General study of the current magnetometer (MAGIC), with the proper components, elements, etc.
4. Determination of topology or components changes.
5. Working improvements for sensors in the areas of noise (better components) and power (lower voltage rail from 17V to 5V)
6. Construction of such sensor using professional manufactured PCB
7. Calibration of such sensor using an already calibrated magnetometer or a special facility.

1.4 Thesis structure

The structure used in this document to present the work done will be the following:

- **Chapter 2: State of the art.** This chapter reviews the general information regarding the most widely used magnetometers for space applications and the basic concepts of space plasma necessary for understanding the type of measurement wanted.
- **Chapter 3: MAG-SPEL Design.** This section focus on each stage of the MAG-SPEL sensor design with simulations, analysis and decision criteria for each topology used.

- **Chapter 4: Results and discussion.** This chapter shows the process of implementation, validation, and calibration of MAG-SPEL so it can be analyses and compared to the previous sensors.
- **Chapter 5: Conclusion.** This section lists the conclusions of the thesis by comparing the initial objectives with the achieved goals, and identifies the future work to be done.

Chapter 2

State of the art

2.1 Types of magnetic sensors and space applications

There are different types of magnetometers. Every model has its own advantages and problems and each must be chosen considering several factors such as: final application, noise, power consumption, size, price, dynamic range and type of measurement. The same magnetometer cannot be used for measuring the body magnetic field and the Earth Magnetic Field. Dynamic range is a very important specification for many applications. Figure 2.1 shows only a portion of magnetometers and sensors and their dynamic range to get an initial idea of each one of them.

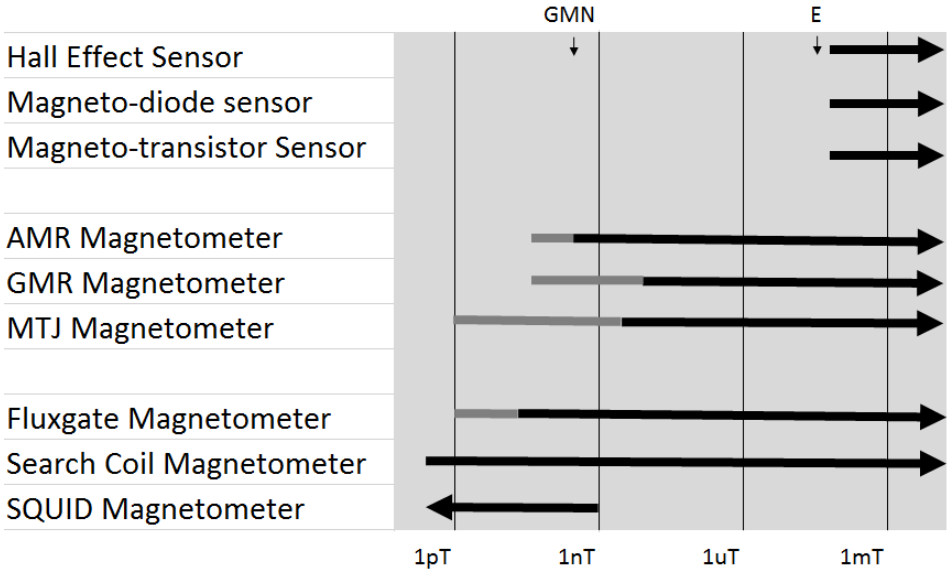

GMN: Geomagnetic Noise. E: Earth's magnetic field

Figure 2.1: Reference table for magnetometers range

Choosing one particular sensor for space research is not an easy task. For example: it is very different a mission created especially for magnetic or plasma research from sending a

sensor in a mission that has other primary objectives. This is the case of CubSats, where the sensor are payloads restrained by the nano-satellite specifications, which are not supposed to change during the process. It is important to know if there is a need of an absolute magnitude or a vectorial sensor that gives information about the direction off the measured magnetic field. Depending on the application one can be more appropriate to the task than the other. There are several reviews on different types of magnetometers and applications [19] [20] which include far more sensors and applications.

In the theme of possible magnetometers several of them can be selected, but as stated above, the application is a crucial point. SQUID (Super Conducting Quantum Interference) magnetometer is incredible at sensing extremely low magnetic fields [21] but with the drawback of using very low temperatures. For this reason, the SQUID sensor is widely used in medicine [22] and particular geophysics applications [23] where temperature control and extreme cooling is at hand. Magnetometers like GMI (Giant Magneto Impedance), Overhouser or hall effect have space applications [24] [15] but are not reviewed because they are not widely used in space applications. This section will present the most relevant magnetic sensors considered for a space based science research on the current SUCHAI 2/3 with a hint of actual implementations in space.

2.1.1 Search Coil Magnetometer

Also referred as "inductive sensor", the search coil magnetometer is a fairly simple sensor as shown on figure 2.2. It relies basically on the use of Faraday Law inside a coil [25]:

$$V_{\mathrm{i}} = \frac{\mathrm{d}\Phi}{\mathrm{d}t} = \frac{\mathrm{d}(NA(t)\mu_0\mu_r(t)H(t))}{\mathrm{d}t} \tag{2.1}$$

Where:

- V_{i} is the voltage induced in the coil.
- Φ is the magnetic flux
- N is the number of turns of the coil around it.
- A is the cross section of the coil
- μ_r is the relative permeability of the sensors core.

A general way to see this equation is by expanding it:

$$V_{\mathrm{i}} = NA(t)\mu_0\mu_r(t)\frac{\mathrm{d}H(t)}{\mathrm{d}t} + N\mu_0\mu_r(t)H(t)\frac{\mathrm{d}A(t)}{\mathrm{d}t} + NA(t)\mu_0 H(t)\frac{\mathrm{d}\mu_r(t)}{\mathrm{d}t} \tag{2.2}$$

The basic induction coils are based on the first two terms (where only $A(t)$ and $H(t)$ are variables). The third term is related to another sensor, the Fluxgate, to be analyzed later. Search coils work by translating variations of H or A into an output voltage. It is a passive component, meaning that no external power is needed for it to work. The existing relation

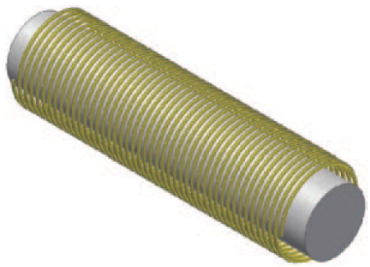

The core can be either a ferromagnetic material or air

Figure 2.2: Search Coil Magnetometer (taken from [1])

between voltage and magnetic field can be measured [1] and analyzed. The core itself can be air or a ferromagnetic core.

As shown on figure 2.1, the search coil has a wide dynamic range and sensitivity, being perfect for measuring Earth's magnetic field and any other event, such as pulsations. It is being widely used for geophysical measurements [26]. It is important to note that any air coil can create or measure a magnetic field, and even measure de magnetic moment of objects located inside them (such is the case with Helmholtz Coils).

The capacitance of the search coil itself can not be neglected at a first order and it depends greatly on the geometry. At low frequency, the voltage output is fairly linear with respect to variations of the ambient magnetic field, and at medium frequencies the current has the same behavior. By using a current-to-voltage converter it is possible to virtually eliminate the effect of the capacitance, achieving more range for the sensor[27][28]. Sometimes a second coil can be added resulting in a two coil magnetometer having a sensing coil and the feedback coil respectively. The feedback coil is introduced to eliminate resonance that the main coil may produce, stabilizing it [29]. Mechanical issues[30] and shielding/grounding[31] of the sensor are also important for an accurate measurement.

The ability for sensing weak magnetic field and the robustness are key elements for this sensor, therefore it is active on space missions even though it can be considered a large size sensor [32][1][33]. Considering the trend for miniaturization, efforts are being made to miniaturize and optimize the power consumption even today[34].

2.1.2 Fluxgate Magnetometer

A vector magnetometer like the search coil, the fluxgate uses the same materials. Consisting in a magnetic core with high permeability, a sensor coil named pick-up coil in this case and a feedback coil named drive coil or excitation coil. The most important equation is:

$$V_{\mathrm{i}} = NA(t)\mu_0 H(t)\frac{\mathrm{d}\mu_r(t)}{\mathrm{d}t} \tag{2.3}$$

This sensors uses variations on the magnetic permeability to measure the ambient mag-

netic field. The difference with a search coil lies in the fact that the fluxgate sensor core is periodically saturated in both polarities[35], increasing the measured reluctance, which is an indicator of the magnetic resistance of the coil, thus creating the effect of a gate for magnetic fields. This type of difference, modulated by the driving current, is measured by the pick-up coil and when the core leaves the saturation zone, more magnetic field will go through the core which is detected again by the pick-up coil. This change of magnetization that happens inside the sensor generates a difference between the input current and output current if there is an ambient magnetic field present.

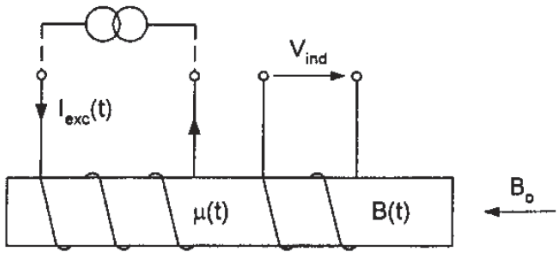

Figure 2.3: Parallel Fluxgate Magnetometer (taken from [2])

The advantages of fluxgate are [2]: they are the best selection for nanotesla range of magnetic field due to the high resolution ($100pT$); high stability with respect to temperature ($0.1nT/C$); no moving parts; noise levels comparable to SQUID device but offering a larger dynamic range, etc.

There are two types of general purpose fluxgates: parallel and orthogonal. Figure 2.3 is the representation of the most common parallel fluxgate, with the driving field having the same direction as measured one. In the orthogonal case, the driving field is perpendicular to the sensitive axis. All analysis from now on will be about the parallel type due to the fact that it has better performance and parameters.

There are several configurations for parallel fluxgates, depending mainly on the core shape, such as:

- Single-Rod: mainly used for time domain detection[36]
- Double-Rod: with two subtypes (Vacquier and Förster). Large portions of the odd harmonics are eliminated in this two-core sensor[37]
- Ring Core: having a pick-up coil with a solenoid form it is the most widely used, being almost regarded as a balance double sensor due to the fact that to half-cores are parts of the closed magnetic circuit [2].

The fluxgate is one of the most used magnetometers for space research. By using the ring core geometry multiple axis measurements can be achieved with extreme simplicity, controlling frequency and feedback field [10]. Missions like the Pioneer 11 [11], BepiColombo [12] and DAWN [13] have used fluxgate magnetometer. COTS versions of the type of magnetometer exist and are the ones with a larger commercial history [9] [14].

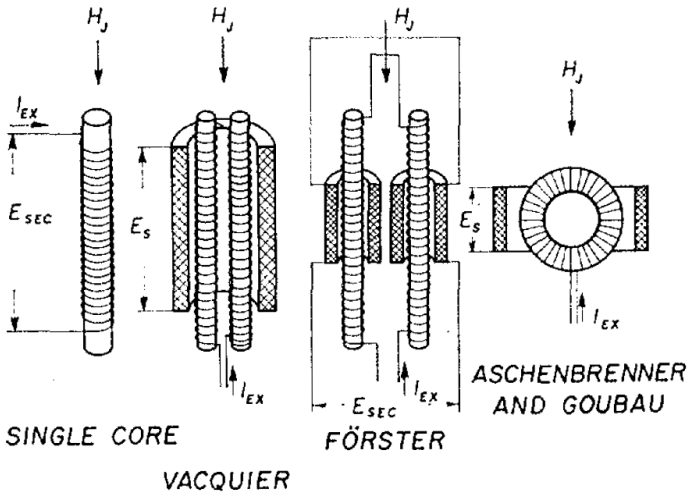

Figure 2.4: Types of Fluxgates (taken from [3])

2.1.3 Magneto-resistive Magnetometer

The magnetoresistive magnetometer (MM) is a device that changes its resistance (ΔR) when in presences of an external magnetic field. This particular device is known for being low cost and simply polarized.

This magneto-resistive effect goes back to Lord Kelvin (Thomson at the time)[39], although the practical application at sensing magnetic field was only achieved a century later, and only in the last three decades research and development enabled the application of such effect on sensors.

Even though several kinds of this particular magnetometer exist (such as: AMR, GMR, MTJ, SDT, EMR, BMR, etc) only the two most relevant to the mission will be presented.

Giant Magneto Resistance (GMR)

This sensor is based on the change of resistance of several materials when in the presences of an external magnetic field. The GMR takes his name on the effect discovered, where changes of magnetoresistance are perceived in planer structures of metal [40]. The structure of the GMR is referred as spin valve and is based on four layers of materials, two ferromagnetic separated by a conductor and an antiferromagnetic material, although some have several layers up to seven or nine.

This structure based on layers makes the GMR a great sensor to be integrated inside a chip, for example BiMOS [41], and the topology of this semiconductors, as in the AMR, is a Wheatstone bridge for maximum output.

It uses different layers that creates an easy path for the electrons to travel depending on the external magnetic field that affects the ferromagnetic layers, being parallel or perpendicular,

suffering less scattering when they change bands from ferromagnetic to ferromagnetic material using the same bands, this effects translates in a different resistance depending on the external field [42] [43].

Although space applications are not the most common use of this sensors, it is widely used on medical applications [44], and the possibility of integration and miniaturization makes it a useful sensor to be considered.

Anisotropic Magneto-Resistance (AMR)

The AMR magnetometer is based on the anisotropic scattering of conduction electrons of the band with uncompensated spins. The energy of the two states of magnetic spin moment ($\pm\mu_B$) differ by the quantum mechanical exchange energy[4]. Due to the anisotropic characteristic of the effect, it is difficult to obtain a general equation that relates the resistance with the magnetic field, because it will depend strongly on the geometry, therefore all materials data have to be found empirically[45].

In reality, by the means of experimental characterization, it is easier: the principle behind it is that the magnetization vector will change when affected with an external magnetic field, prompting a change on the overall resistances of the device. This change on the resistance is measured by an external circuit. The effects of an external magnetic field are quantifiable for this type of sensor, thus the transfer function usually has the following form:

$$R = R_0 + 2\Delta R_0 cos2\theta \tag{2.4}$$

Where θ is the angle between the magnetization and the current inside each resistor as shown on figure

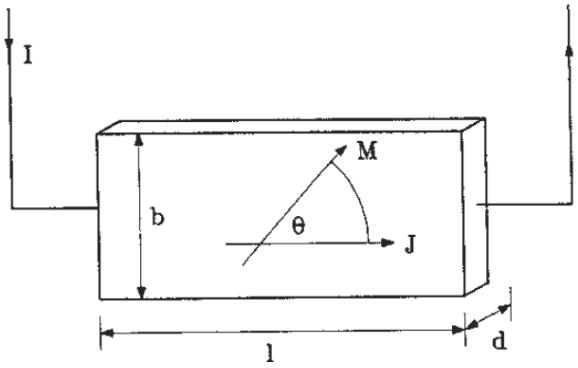

Representation of a simple AMR magnetometer: thin-film with magneto-resistive proprieties

Figure 2.5: Current and magnetization on a thin-film strip (taken from [4])

Due to the nonlinear characteristic of 2.4, there are several techniques to linearize the output signal[4]:

- Perpendicular Bias
  - Permanent magnetic films to stablish an angle $\theta > 0$
  - Exchange couple films: where a unidirectional anisotropy is induced by exchanging coupling of the AMR film with an anti-ferromagnetic of ferromagnetic layer.
  - Shunt bias, which works by shunting the current arranging the AMR layer with insulating layers and non-magnetic conductors.
- Longitudinal Bias
  - Hard magnetic films: by adding high coercivity thin films, providing a magnetization and thus a bias
  - Exchange tabs: where the end zones domains are pinned by exchange coupling (like in perpendicular bias).
- Geometric Bias
  - Herringbones: where the rectangular element is geometrically inclined with a Φ angle with respect to the measurement axis
  - Barberpoles: where thin-film metal with high conductivity are added to create a 45 degrees' angle between the magnetization and the current

The most important part of the AMR is how much the resistance can change, hoping for a large coefficient $\Delta\rho/\rho$. This sensors are mostly build using alloys (such as Ni, Fe and Co) or permalloys. These magnetometers are widely used in space mission that need a magnetometer of low resources and without a stunning sensitivity. Examples of missions are the Tatiana-2 [46], SOSMAG[47] and TRIO-CINEMA [17]

Sensor HMC1001

The HMC1001 sensor is build based on a Wheatstone bridge of equal resistances on all axis. It is considered a Magnetoresistive Magnetometer (MM), specifically an Anisotropic Magneto Resistance (AMR). The MM is a device that changes his resistance (ΔR) when in presence of an external magnetic field. This particular device is known for being low cost and simply polarized. It is composed of four permalloys (nickel iron magnetic alloy) arranged in a Wheatstone bridge [48] as shown in figure 2.6a

The DC voltage of the two outputs should be $V_{bridge}/2$ if all parameters are ideal. In reality this might be quite different due to:

- Construction of the sensor, which might result in different resistance of each part of the bridge, resulting in a different DC output voltage
- Different sensibility of each resistance and different offset of this sensibility

A remarkable characteristic is also shown in figure (2.6b), where the different permalloys are magnetized from the factory with an internal coild for set/reset purposes. This means that the permalloys can be saturated on either director, giving the sensor a larger output and helping with the unwanted effects of DC noise or offset, and also helping with the sensor stability [49]. These set/rest straps also have the effect of modulating the ambient magnetic

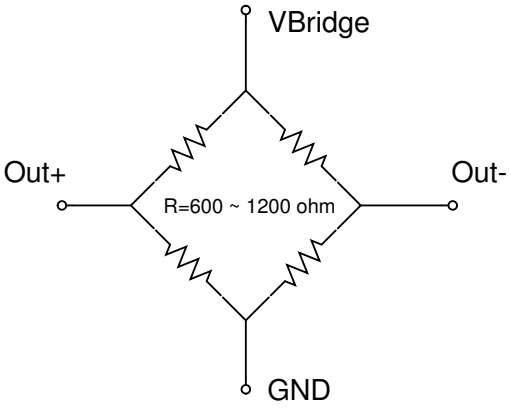

(a) HMC1001 Wheatstone Bridge

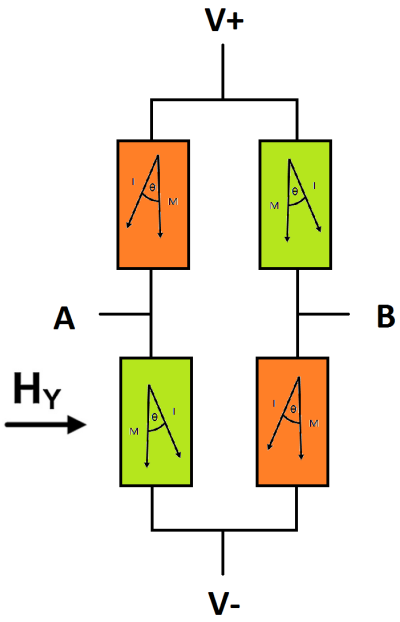

(b) Current and magnetization direction

Figure 2.6: Wheatstone bridge topology of the sensor and magnetization directions

field with a square signal. This process is known as flipping [49]. There are many advantages of using this process, which is equivalent to chop the output signal between negative and positive magnetic measurements. This process is the most important one because it moves the signal from high flicker noise to a whiter noise spectrum.

As shown in equation (2.4) the response of this device is non-linear, but a particular technique is used for the linearization: barber poles.

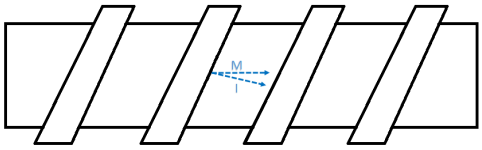

Figure 2.7: Barber poles in the sensor construction

Figure 2.7 shows the topology of barber poles inside the permalloy, they are designed as conductive shunts form by Au stripes. This stripes helps with the linearity by forcing the current inside to go with a 45^o or -45^o orientation with respect to the default magnetization [50][51], incidentally this is the most linear point in the $cos^2\theta$ function. The different directions that the barber pale takes generates a greater output, helping with noise reduction.

2.2 Magnetometer from Imperial College

As a result of this review a suitable choice for our cubeSat mission is selected. MAGIC (Magnetometer of Imperial College) from the TRIO-CINEMA [17] [16] mission presented a

very small magnetometer for space research that uses the HMC1001 sensor. MAGIC has good qualities that fit the current mission of Universidad de Chile. Thus, it was selected as a model to follow in which a COTS magnetometer is used. The general topology of the electronics is shown in figure 2.8

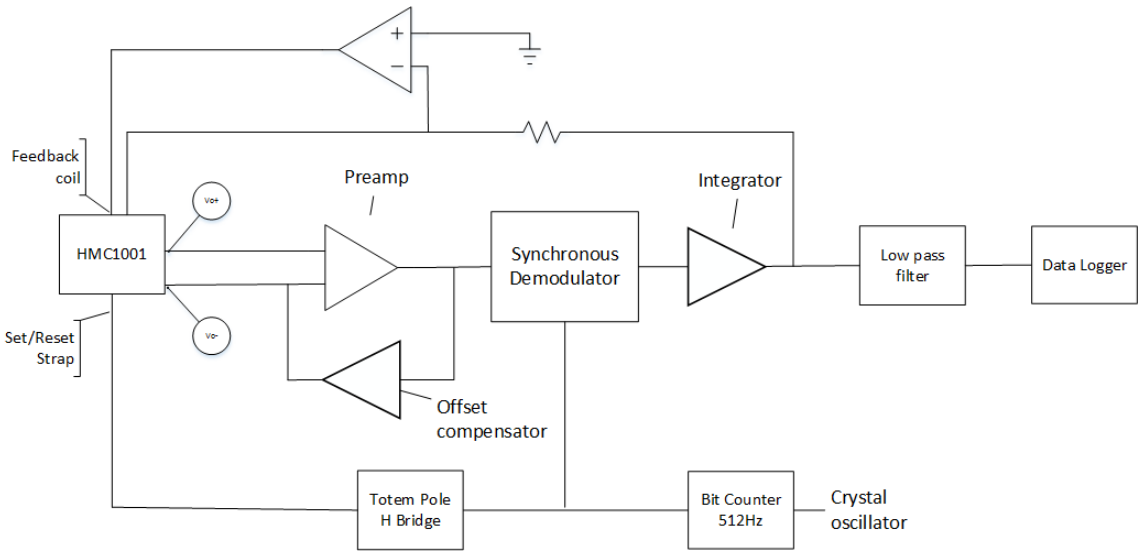

Figure 2.8: MAGIC circuit to be replicated

This magnetometer has the following specifications given by [17]:

Instrument specifications	
Mass	104g (total)
Volume	Sensor head 10 cm^3
	Electronics 173 cm^3
Dynamic range	$\pm$ 57 500 nT
-3dB point	16Hz
Operational temperature	-50^oC to $+60^oC$ (electronics)
	-120^oC to $+80^oC$ (sensor)
Flipping frequency	512Hz
Sensitivity	2nT
Vectors	32
Decimation	324
Bus rails	17V, 5V, 3.3V
Power	425mW

2.3 Magnetic Pulsations

Magnetic pulsations are the earth surface manifestation of ultra low frequency (ULF) hydromagnetic waves originally called micropulsations. These pulsations did not have a theoretical and accepted explanation until it was proposed that they were caused by stationary Alfvén waves[52].

The origin of these pulsations comes from the interplanetary medium, the magnetosphere dynamic and the sun itself. The amplitude measured over the earth surface is substantially different from measurement in the magnetosphere., since:

- Energy that is transformed during the process
- Radiation added by the currents in the ionosphere
- Effects of the ionosphere itself on the passage of electromagnetic waves.

These pulsations generally have frequencies between $f \approx 1$ mHz and $f \approx 10$ Hz. Where the largest ones are given by the gyrofrequency of hydrogen and the lowest are given by the time of propagation through the magnetosphere. On land, this is reflected in variations from 0.1 nT at high frequencies to tens or hundreds of nT at low frequencies, generally becoming larger in magnitude as latitude increases. A detailed classification of these waves was made by the Association of Geomagnetism and Aeronomy (IAGA):

Table 2.1: AIGA Classification for different types of magnetic pulsations

	T(s)	Frequency	Sources
Pc1	0.2 – 5	High:	Ion-cyclotron instability
Pc2	5 – 10	0.1 – 10 Hz	in magnetosphere.
Pc3	10 – 45	Mid:	Proton-cyclotron
		10 – 100 mHz	instability in the SW;
			Kelvin–Helmholtz instability.
Pc4	45 – 150	Low:	Kelvin–Helmholtz instability;
		1 – 10 mHz	Drift-mirror instability;
Pc5	150 – 600		Bounce resonance.
Pi1	1 – 40		Field aligned current
			driven instabilities.
Pi2	40 – 150		Abrupt changes in convection
			in the magnetotail;
			Flux transfer events.

Magnetic pulsations depend on magnetospheric processes and their interconnection with the ionosphere, the solar wind (SW) and the interplanetary magnetic field (IMF), depending strongly on the latitude. Dungey[52] also introduced the concept of Field Line Resonance (FLR), a basic process for understanding these pulsations and identified Kevin Helmholtz instability (KHI) in the magnetopause as an energy source for them.

With this information, a small table can be made with the different types of pulsations:

2.3.1 Magnetic fields with axial symmetry: dipole case

The equations that rule the magnetic pulsations behavior and the ones used for such analysis are directly related with magneto hydrodynamics (MHD) equations[53]. Passing the problem to MHD waves in an axial symmetry we can obtain a better approximation of the magnetosphere and the relations that are key for understanding its behavior. For this,

Table 2.2: Magnetic pulsations characteristics

	Period	**frequency**	**Amplitude** (mid latitudes)
Pc1	0.2-5s	0.2-5Hz	0.01-0.1nT
Pc2	5-10s	0.1-0.2Hz	1nT
Pc3	10-45s	20-100mHz	1nT
Pc4	45-150s	7-22mHz	1nT
Pc5	150-600s	2-7mHz	40-400nT

cylindrical coordinates (r, ϕ, z) will be used. The magnetic field will then be given by a stationary field B_0 with the exception that, given the geometry, $B_0 = (B_r, 0, B_z)$. In addition, $\frac{\partial B_{0r}}{\partial \phi} = \frac{\partial B_{0z}}{\partial \phi} = 0$ Thus, the general MHD equations can be written as:

$$\left[\omega^2 \mu_0 \rho_{m0} - \frac{1}{r}(\vec{B}\cdot\vec{\nabla}) r^2 (\vec{B}\cdot\vec{\nabla})\right]\left(\frac{U_\phi}{r}\right) = \omega m (\frac{\vec{B}\cdot\vec{b}}{r}) \tag{2.5}$$

$$\left(\omega^2 \mu_0 \rho_{m0} - r(\vec{B}\cdot\vec{\nabla})\frac{1}{r^2 B^2}(\vec{B}\cdot\vec{\nabla})\right)(rE_\phi) = \mathrm{i}\omega B^2 (\vec{B}\times\vec{\nabla})_\phi (\frac{\vec{B}\cdot\vec{b}}{B^2}) \tag{2.6}$$

$$\mathrm{i}\omega(\vec{B}\cdot\vec{b}) = \frac{1}{r}(\vec{B}\times\vec{\nabla})_\phi (rE_\phi) - \mathrm{i}mB^2\frac{U_\phi}{r} \tag{2.7}$$

Where the variations were made from the form $\exp(\mathrm{i}m\phi - \omega t)$. The transition from the general equations of MHD to the final ones is not intuitive and was not developed in detail as the results are achieved in the literature and given by the developments of Dungey. A more explicit way of writing these equations is given by:

$$\left[\frac{\omega^2}{V_A^2} - \frac{1}{rB_0}\vec{\nabla}_{||}(r^2 B_0 \vec{\nabla}_{||})\right]\left(\frac{U_\phi}{r}\right) = \frac{\omega m}{r^2}\frac{b_{||}}{B_0} \tag{2.8}$$

$$\left[\frac{\omega^2}{V_A^2} - r^2 B_0 \vec{\nabla}_{||}(\frac{\vec{\nabla}_{||}}{r^2 B_0})\right](rE_\phi) = -\mathrm{i}\omega B_0 r \vec{\nabla}_\perp \frac{b_{||}}{B_0} \tag{2.9}$$

$$\mathrm{i}m\left(\frac{U_\phi}{r}\right) + \frac{1}{rB_0}\vec{\nabla}_\perp (rE_\phi) = \mathrm{i}\omega\frac{b_{||}}{B_0} \tag{2.10}$$

Where $\vec{\nabla}_{||} = \hat{\mathrm{e}}_{B_0}\cdot\vec{\nabla}$ and $\vec{\nabla}_\perp = (\hat{\mathrm{e}}_{B_0}\times\vec{\nabla})_\phi$

These equations have been the subject of large discussions, but their meaning can be discussed with a little review. The left side (LHS) of 2.5 and 2.6 (2.8 and 2.9) have the form of a one-dimensional wave where the unique spatial derivative is given by $\vec{B}\cdot\vec{\nabla}$, being a derivative along $\vec{B}$. These equations are coupled on the right-hand side (RHS), which depends directly on the compressional component $\vec{B}\cdot\vec{b}$. The equation 2.7 (2.10) shows the union between the latter, E_ϕ and U_ϕ, closing the system.

Studying the limits of each equations then gives birth to each mode of propagation.

2.3.2 Modes of propagation

If the wave has axial symmetry (axisymmetric), which means that the waves are in phase throughout ϕ, $m = 0$ with which the right side of 2.5 (2.8) disappears leaving:

$$\left[\frac{\omega^2}{V_A^2} - \frac{1}{rB_0}\vec{\nabla}_{||}(r^2 B_0 \vec{\nabla}_{||})\right]\left(\frac{U_\phi}{r}\right) = 0 \tag{2.11}$$

This corresponds to the toroidal mode since it remains a uni-dimensional wave with spatial derivative along B_0 with all the characteristics of the mode of Alfvén. Generally speaking, this wave is the cause of East-West disturbances. In this case, both $\vec{b}$ and $\vec{U}$ are azimuthal and the electric field E is normal to the field lines.

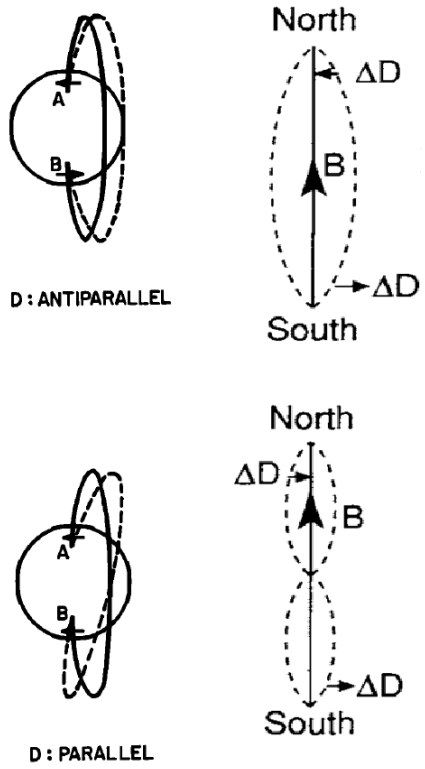

It can be seen how in the toroidal mode the magnetic field line is displaced azimuthally. The view is towards Earth with the lines from south to north, thus having disturbances of east-west type

Figure 2.9: Example of toroidal mode on an Earth like object

On the other hand, the equation 2.6 (2.9) shows another mode, where E is azimuthal and both U and b are in the meridional plane and the whole cavity resonates coherently. This feature is known as cavity mode or general poloidal mode. In general terms, this mode would be the cause of the radial and north-south disturbances and has all the characteristics of a fast magnetosonic mode.

The other limit ($m = \infty$) is so that the equation 2.5 (2.8) can only exist if the perturbation b is perpendicular to the magnetic field without a parallel component. This results in a transverse mode where the wave propagates along B_0, reason why it is called guided poloidal mode, since E is azimuthal and both u and b are perpendicular to the lines of field but in the same plane of this.

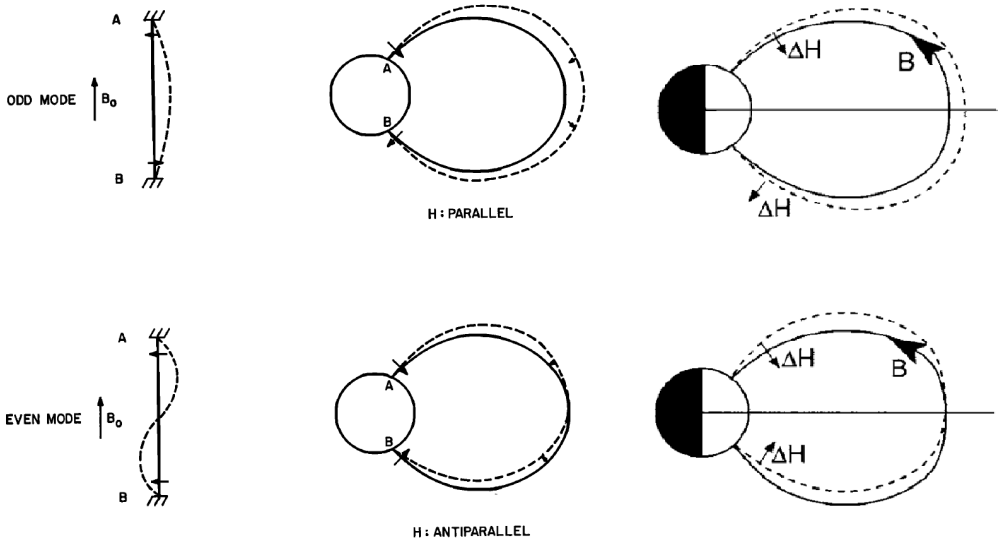

It can be seen that in the poloidal mode (specifically the guided poloidal mode) the magnetic field line is displaced on the same meridian, whereby all perturbations are in fact radial in the guided case. In the case of a generic poloidal mode, perturbations can go in any direction within the same meridian

Figure 2.10: Example of poloidal mode on an Earth like object

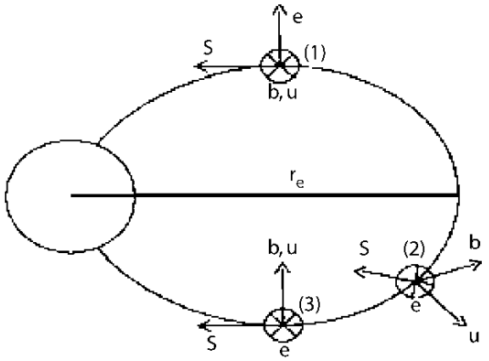

In this case, the three modes can be seen separately: toroidal mode (1), guided poloidal mode (3), and cavity (or general poloidal) mode (2)

Figure 2.11: Example of all three modes on an Earth like object

2.3.3 PC5 waves

Given the particular interest of designing a sensor as low cost as possible, it is important to see which wave to measure and where. Given the table shown in 2.1 it can be inferred that PC5 waves would be the best option to be measured. There are encouraging elements since a classic fluxgate has a resolution of 0.1nT, whereas a normal CubeSat sensor has only about tens of nT. One factor that again contributes to this is the fact that they increase with latitude, having their maximums at the poles, which given a polar orbit, helps.

As a summary of the above information, the important elements of a PC5 wave are:

- Frequencies from 1 mHz to 10 mHz
- Caused mainly by:
  - KHI
  - FLR
- They have increased amplitude as they approach the poles

It is also important to note that there are three modes of PC5: toroidal, compressional (cavity mode) and poloidal. Data indicate that the compressional component of PC5 would be the easiest to measure since it would have a higher power.

PC5 Compressional waves were reported in space in 1969 and typically exhibit large variations, in the order of $\delta B/B \approx 0.2 - 0.5$ being quasi sinusoidal. This compression is generally accompanied by a radial variation of equal magnitude, the toroidal being 5 times smaller. Thus, the toroidal component is related to FLR while the compressional is directly related to ion injection (SW)

On the earth surface the maximum intensity of these can reach 400nT at low frequencies and tend to be positioned at the oval aurora, between latitude angles $\pm 69^0$ to $\pm 89^0$

Distribution of PC5 [54][55]

Initially the PC5 compressional waves were measured at $L > 8$, where L is the distance between the field line (or cavity) to the equator, measured in radios of the earth, indicating an origin near the magnetopause, having greater occurrence at dawn and dusk. In geosynchronous orbits ($L \approx 6.6$) the waves were observed propagating away from noon on both sides of the magnetosphere, which is consistent with KHI. An L/LMT plot can be obtained as it is shown on figure 2.12

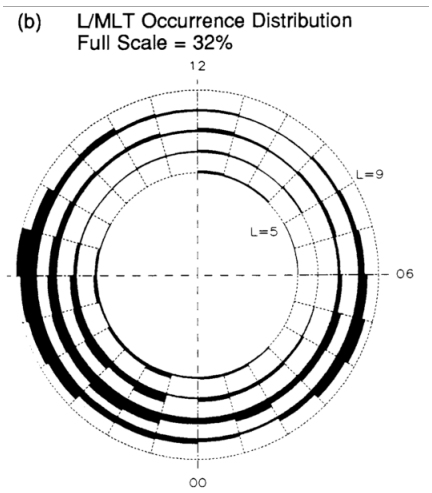

Distribution in magnetic latitude as a function of distance L / LMT. LMT is local magnetic time, defined as the geomagnetic length of the observer minus the geomagnetic length of the sun expressed in hours plus 12

Figure 2.12: L/LMT occurrence distribution of compressional PC5 waves

From where the first problem arises: the important amplitudes of PC5 are usually outside L = 7. Far from where it will be measured, theoretically, with a CubeSat if the measurements are made at the equator. Thus, it is important to remember that all measurements will be made at the poles.

On the other hand, toroidal PC5 is generally at distances of L = 5-9 as shown in figure 2.13

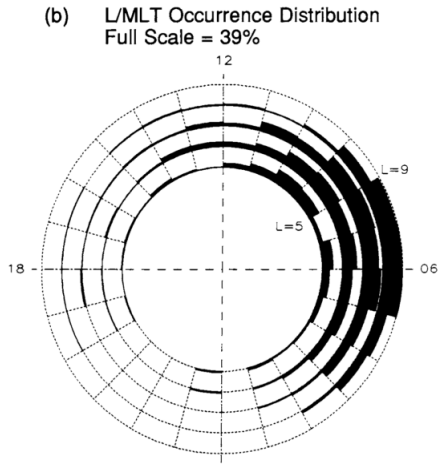

Figure 2.13: L/LMT occurrence distribution of toroidal PC5 waves

Chapter 3

MAG-SPEL Design

The technical criteria used for deciding that MAGIC and an HMC magnetometer are the solution were:

Highly sensitive configuration. The HMC1001 was designed especially for low field magnetic sensing. Using the on-chip straps such as "Set/Reset" and "Offset", it is possible to create a negative feedback turning the sensor in a null detector. This reduces the noise by changing the magnetization of the permalloy with periodic-bipolar electric pulses [48]. Therefore, by using this flipping technique, the output is optimized in terms of signal to noise ratio, removing the effect of hysteresis and helping with the resistances of the sensor itself [49].

Low noise in the band of interest. In this case the frequency band that will be analyzed is very close to DC (0.1Hz - 10Hz), which has a predominant flicker noise with a 1/f spectrum noise [56]. All electronics have flicker noise because it is intrinsic to every electronic component. A study about the low frequency noise was completed and the HMC1001 had the lowest noise spectrum at the frequencies of interest [57]. Therefore, this specific magnetometer is a competitive option for a CubeSat mission.

Commercial Price. In the history of space based magnetometers, fluxgates were generally constructed considering all the requirements of that mission and for the sole purpose of it and it is usually custom made, increasing the price and the time spent waiting for the sensor to arrive. The HMC1001 is a COTS chip that can be bought online and delivered in 8 days approximately with a reasonable price (USD $ 20), a huge advantage considering the budget of a small mission and the times of development.

Size. The magnetometer is scheduled to be lunched inside a CubeSat of 3U which has several other sensor and research equipment inside. Considering this, the fluxgate size is no adequate for a small satellite mission due to the size, even considering the new COTS versions of it. The HMC1001 has a size that is approximately of $(10mm)x(7mm)$ [48] making it considerably smaller than a fluxgate and perfect for the current mission.

Power consumption. This particular topology needs a periodic-bipolar current pulse of roughly 5A to work at the best operating point, which could be translated in a higher

power consumption. The target magnetometer, MAGIC, has a nominal consumption of approximately 400mW in science mode for each axis. Different types of magnetometer may be able to reduce this value [11] but a general 1W power consumption is good for a CubeSat with a 5 W maximum power. This criterion comes as a key factor when talking about the target resolution, which increases with the power consumption.

The sensor is configured as a null detector in order to force the error to be as close to zero as posible. As the HMC1001 sensor is driven by the bipolar current pulses on the set/rest strap, a square signal would be the theoretical output. This means that the amplitude of such signal would be directly related to the magnetic field measured. The sensor design is shown in figure 3.1 and it can be divided into five different stages:

1. HMC1001 sensor.
2. Offset compensation and gain stage.
3. Demodulation.
4. Integration and feedback.
5. Current pulse generator.

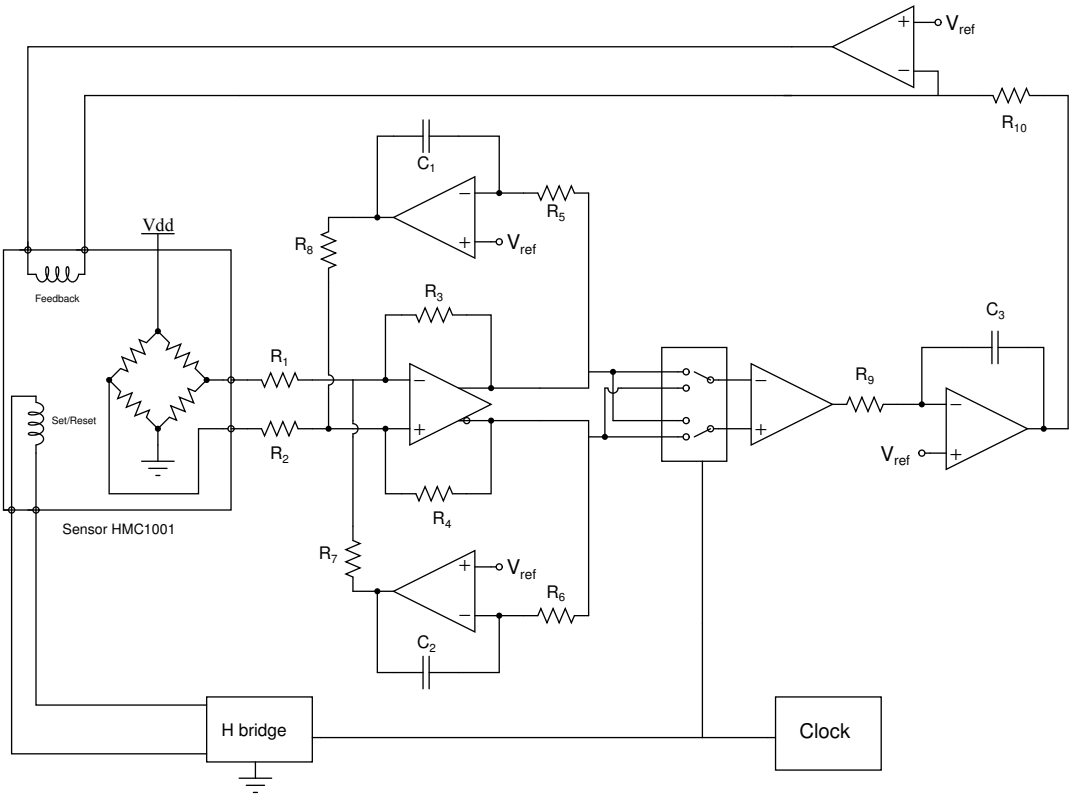

Figure 3.1: MAG-SPEL design

3.1 Stage analysis

3.1.1 HMC1001

In order to work with initial settings for the HMC1001, simulations were made to choose topologies and values while having an initial and approximate idea of the overall operation. Simulations also give an initial insight to each stage functionality and expected output voltage in a control environment. No current feasible simulation scheme can easily replicate the magnetic feedback and hysteresis of the sensor with a simple SPICE circuit, although a mathematical model has been developed[58]. Considering this issue, and the objective of each simulation, a simple abstraction for the sensor HMC1001 is presented on figure 3.2.

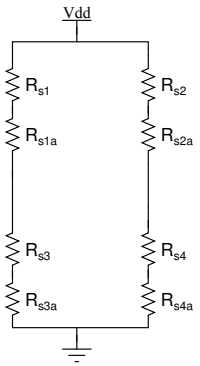

Figure 3.2: HMC1001 Wheatstone Bridge abstraction

The set/reset and feedback coil are not considered in this model. R_{s1}, R_{s2}, R_{s3}, and R_{s4} are the nominal resistances of the each branch of the sensor, with a component that fluctuates imitating the presence of a magnetic field and a set/reset behavior represented by R_{s1a}, R_{s2a}, R_{s3a} and R_{s4a} respectively. This gives the chance to analyze the possibility of slightly different sensibility of each resistor and also a mismatch in values at zero field that feeds the rest of the circuit. Thus, the effect of the magnetic field can be added to the model shown on figure 3.2 by making the resistances dependable of an independent voltage source. With such technique, no current pulses are needed on simulation and several cases can be studied.

3.1.2 Offset compensation and gain stage

Due to the modulation of the signal a possible offset mismatch can occur. The first stage has to solve any issue with this by eliminating the offset for a proper signal handling. An initial solution for the problem was to use mathematical formulas and simple amplifiers to add and subtract signals. Just by this method it is not possible to eliminate the DC offset because each signal might have different offsets:

$$V_{out1} = v_1 + v_{off1} \tag{3.1}$$
$$V_{out2} = v_2 + v_{off2} \tag{3.2}$$
$$V_{out1} - V_{out2} = v_1 + v_{off1} - (v_2 + v_{off2}) \tag{3.3}$$
$$= v_1 - v_2 + (v_{off1} - v_{off2}) \tag{3.4}$$

Therefore, the offset signals would only be compensated if they have the same offset, which is not realistic. Thus, a more extensive design must be used. As seen on [17], the first stage of the sensor is a preamp of high gain and an offset compensation build with a feedback block as an integrator. In the case of a single ended type topology, the circuit is as shown on figure 3.3.

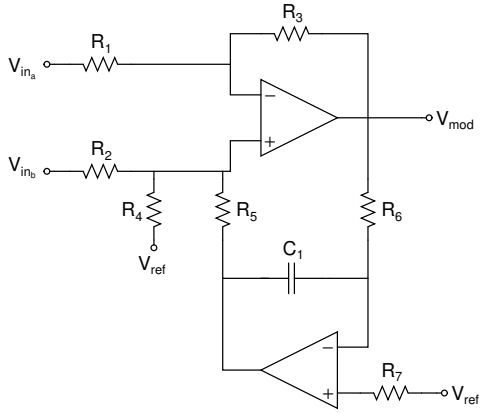

R_1 and R_2 are only added for gain stabilization compared to the MAGIC design

Figure 3.3: MAG-SPEL Offset/amplification initial stage design

Such topology has the problem that it initially transforms a differential signal into a single ended one, thus creating a problem for the demodulation stage that now has to demodulate a single ended signal. A simple solution to such problem is to use the circuit shown on figure 3.4

With this, the stage works as a fully differential amplifier with an offset compensation feedback using two integrators in a positive feedback (one for each side of the differential amplifier), than subtracts only the DC value of the voltage. A trade off appears due to this RC constant and is important to consider it, a large value will have a smaller effect on the AC signal but will generate a larger settling time for true value. It is important to notice that R_8 and R_7 resistors are of a small value, so that current noise is not amplified by the loop. The frequency for flipping was set to 490Hz and the RC constant of both integrators was set to 0.1Hz. This topology also gives the benefit of redundancy: if one integrator fails, the stage will still work with one feedback loop, with a slower settling time.

The main reason for using a fully differential amplifier and keep a differential signal after the gain stage is to have a smoother demodulation stage, which is further explained on the demodulation section.

An important factor for this kind of stage is the stability of it due to the positive feedback.

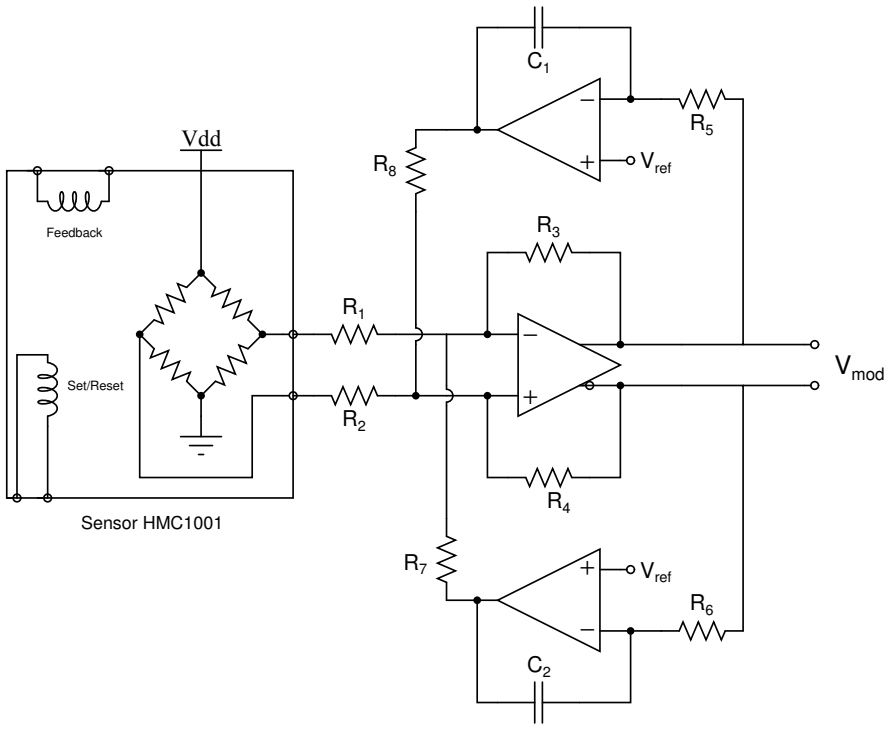

Figure 3.4: MAG-SPEL Offset/amplification final stage design

This stage is characterized as being a band pass filter made specifically so that the desire frequencies are not affected by the operation as shown in figure 3.5.

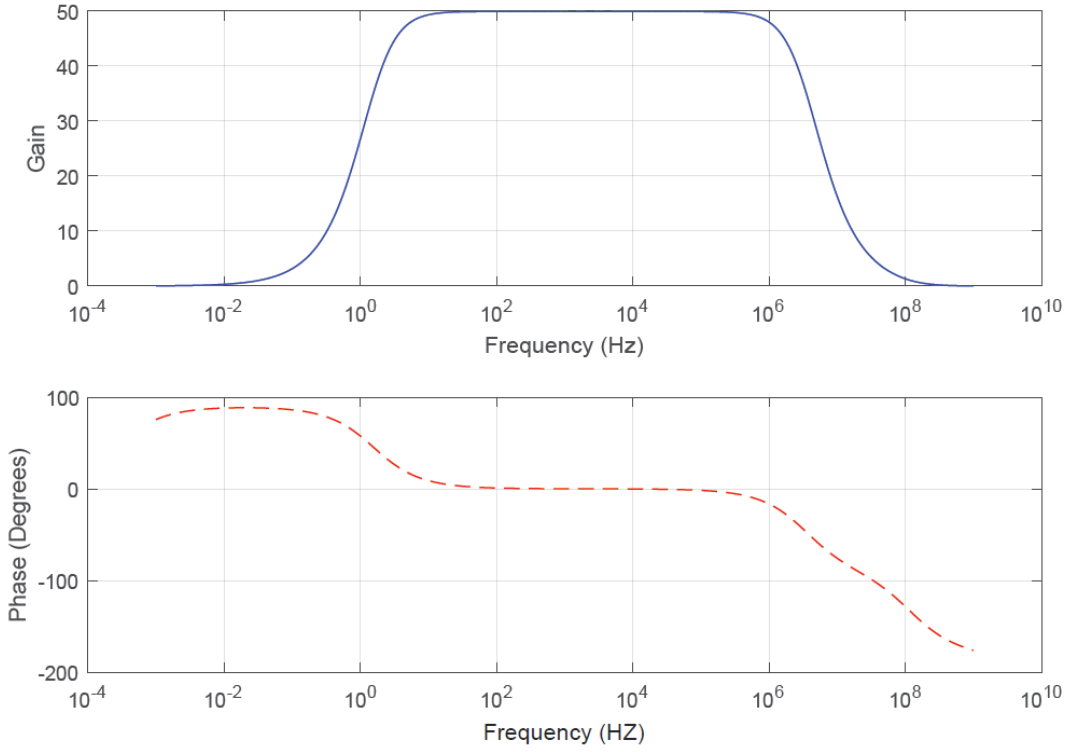

Figure 3.5: AC SPICE simulation for the Offset/amplification stage

Using the method proposed by R. D. Middlebrook [59][60] it is possible to obtain stability characteristic of the circuit in a open loop scheme, resulting in:

- Crossover frequency is 0.7895980 Hz
- Phase Margin is 89.999774 degrees
- Gain at phase crossover frequency is $-142.22981 \mathrm{d}B$

Thus, the system is stable, it has only the pole of the integrator affecting the output signal as shown by the almost 90 degree' phase margin.

3.1.3 Demodulation

The goal for this stage is to create a synchronous demodulator using only switches and OPAMPs. The input signal of this stage has the form shown on figure 3.6

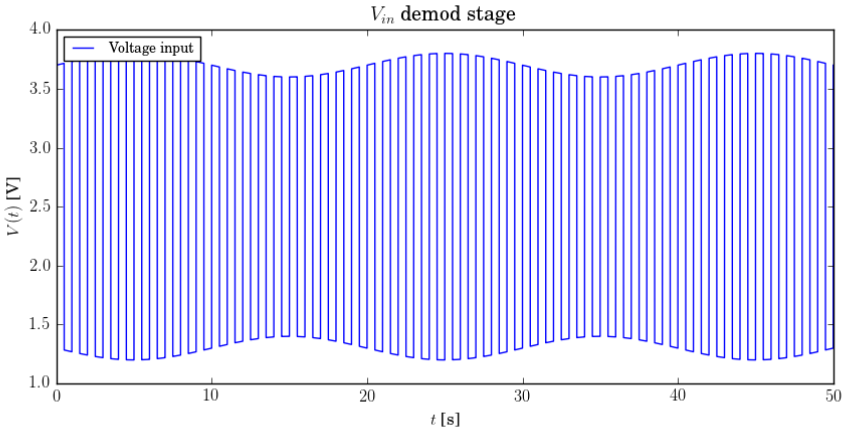

Figure 3.6: Example of the offset/amplification stage output signal

The first possible solution is using an amplifier that switches between a gain of 1 and -1 in synchrony with the sensor as shown on figure 3.7

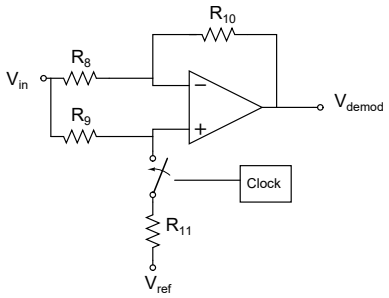

Figure 3.7: MAG-SPEL Demodulation initial stage design

In this case all resistances are considered to be equal ($R_8 = R_9 = R_{10} = R_{11} = 10k\Omega$) This demodulator has two states with different outputs, when the switch is open the output is:

$$V_{out_1} = V_{in} \frac{\frac{R_8}{R_8 + R_{10}}}{\frac{1}{A} + \frac{R_8}{R_8 + R_{10}}} \tag{3.5}$$

Where A is the open loop gain of the amplifier. When the switch is closed the output is:

$$V_{out_2} = V_{ref} \frac{1}{\frac{1}{A} + \frac{R_8}{R_8 + R_{10}}} - V_{in} \frac{R_{10}}{R_8} \tag{3.6}$$

By assuming that $A >> 1$ and that all the resistances are equal, the output voltage becomes:

$$V_{out_1} = V_{in} \tag{3.7}$$

$$V_{out_2} = 2V_{ref} - V_{in} \tag{3.8}$$

The results shows that the signal is demodulated, changing the total gain from 1 to -1 effortless. But, due to the several approximations done to the resistances values and gains, this could be different. Considering that the resistors used have a 1% tolerance, it is possible to estimate errors that arise due to this process.

For example: if the resistors have each a 0.5% error on opposite directions of a 10 $k\Omega$ resistance (i.e 10.05 $k\Omega$ and 9.95 $k\Omega$), an output signal of such stage would look like figure 3.8. This case assumes a 4000 nT field oscillation modulated at the leve of the earth magnetic field.

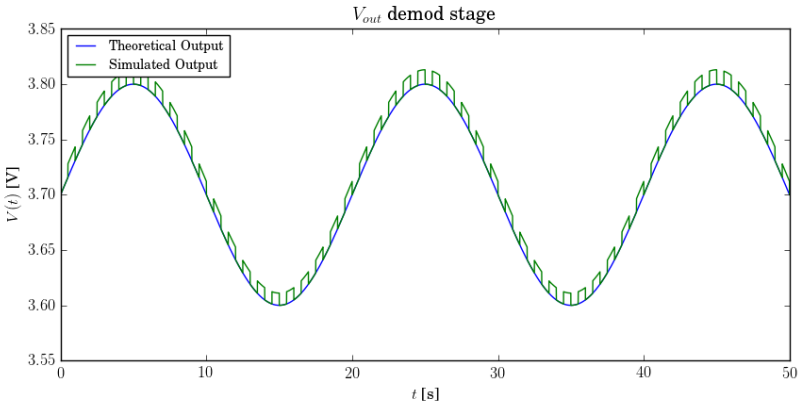

Figure 3.8: Output signal of the demodulation stage, theoretical and simulated

It is clearly visible that a small error on the resistors does create a significant error on the output signal. If this error is isolated and then compared to the signal itself, it is possible to appreciate the magnitude it can have.

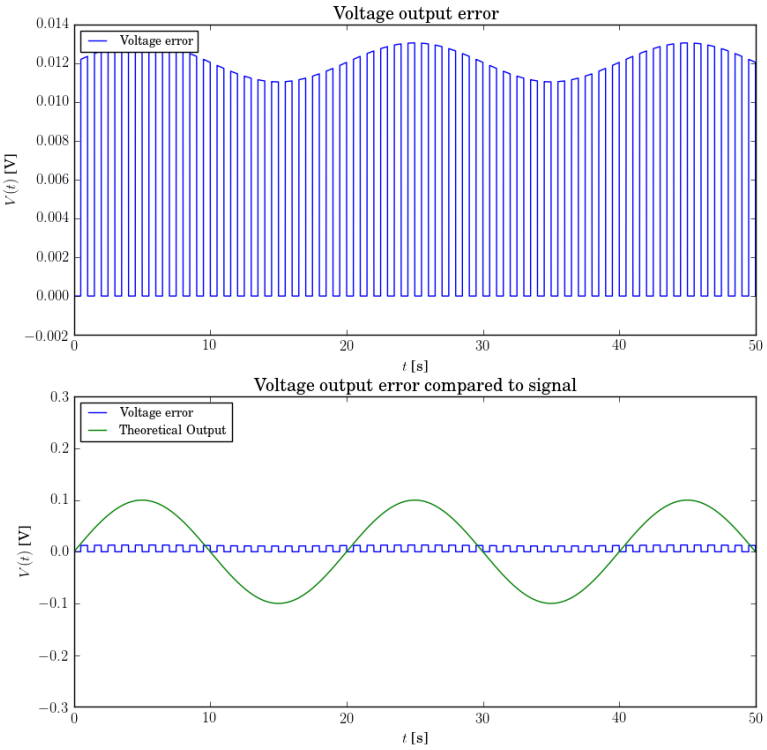

Top: Difference between simulated and theoretical demodulator output.
Bottom Comparison of error and theoretical output signal

Figure 3.9: Error related to the demodulation stage

A porcentual error plot shows on figure 3.10 how, in this particular case of a large signal, the error can be up to 15%. This error increases with a smaller signal, and considering that a PC5 signal wave has about 400 nT swings, the error is considerably large in such case.

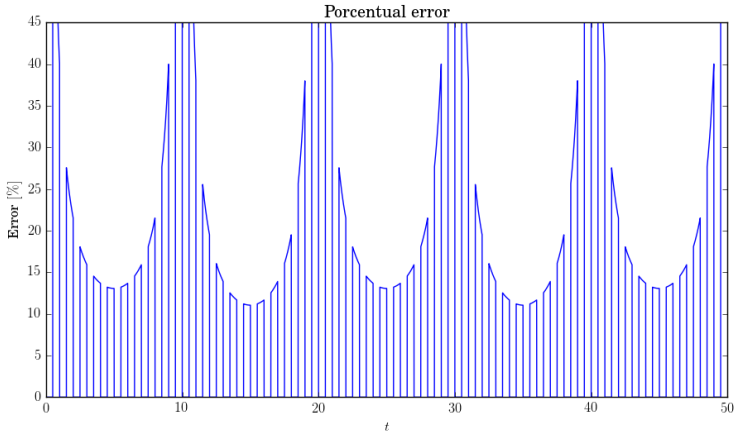

Figure 3.10: Percentage of the error relative to the theoretical signal

A way to avoid such problems is to assume that the following integrator will completely

eliminate any trace of this noise. This solution puts more stress on the performance of such integrator, which is a key element of feedback. Another way to solve it is to work with the idea of differential signals that was introduced for the previous stage. An instrumentation amplifier set with a gain of 1 together with a double DPST (double-pole, single-throw) switch can achieve a smooth demodulation, forcing any gain error to be applied to both differential signals, and minimizing the signal error. The circuit on figure 3.11 shows how the gain and demodulation stage looks like together.

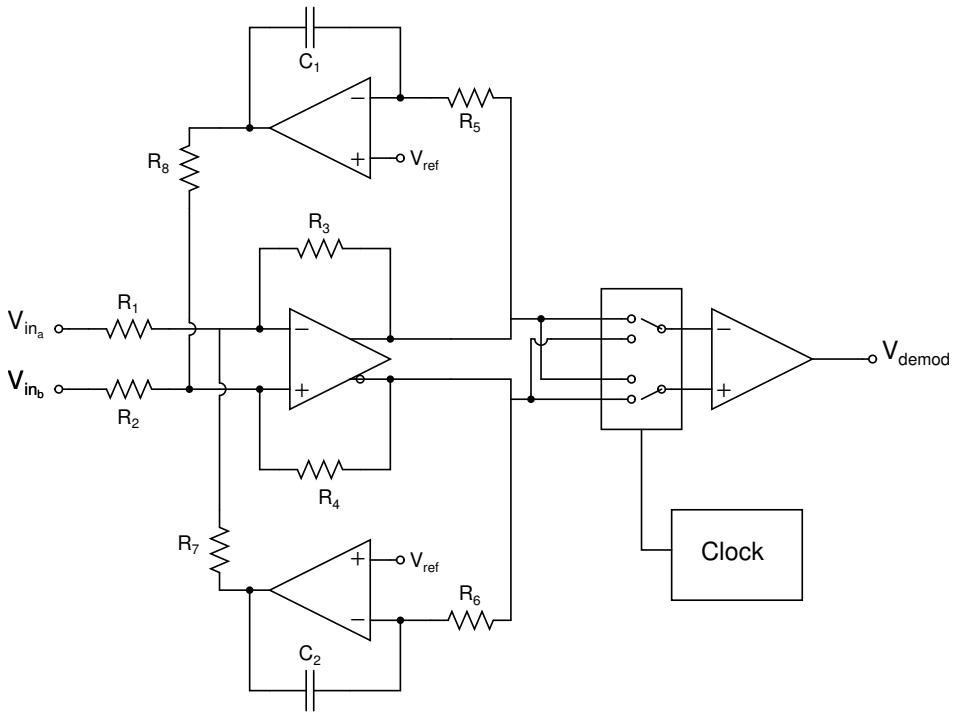

Figure 3.11: MAG-SPEL demodulation final stage design

At this point the AC signal has been demodulated and the single ended voltage is proportional to the ambient magnetic field measured by the HMC1001 sensor.

3.1.4 Integration and feedback

The integrator that follows works with the voltage to current generator that is connected to the offset strap, which creates a negative magnetic field to counter the ambient field inside the sensor. As the integrator changes the voltage due to the ambient noise, the feedback coil forces the HMC1001 output to be zero. The integrator is then forced to stop working and this achieves an output voltage equal to the one needed for the sensor to measure zero. This feedback also improves linearity and temperature drift of the sensor[17], and through R_{10} the dynamic range of the whole system can be set to a desire value thanks to the control over the feedback current.

3.1.5 Current pulse generator

The bipolar current pulses are generated with the circuit shown in 3.12. This circuit is a H bridge that uses the set/reset straps as a load in series with a bulk of capacitors. These capacitor are the ones able to create the short time pulses. The RC constant generated due to this configuration will determinate the pulse duration. The supply voltage in this case was set to 15V by using a DC-DC converter from the 5V CubeSat rail. Shunt resistors were added to control the RC constant and obtain measurements of this pulses. This stage generates current pulses of >5A, which are large enough to reorganize the magnetic domains of the HMC1001. Capacitors C_1 though C_7 and resistors R_1 through R_3 were added to filter the power supply and relief stress from the DC-DC converter.

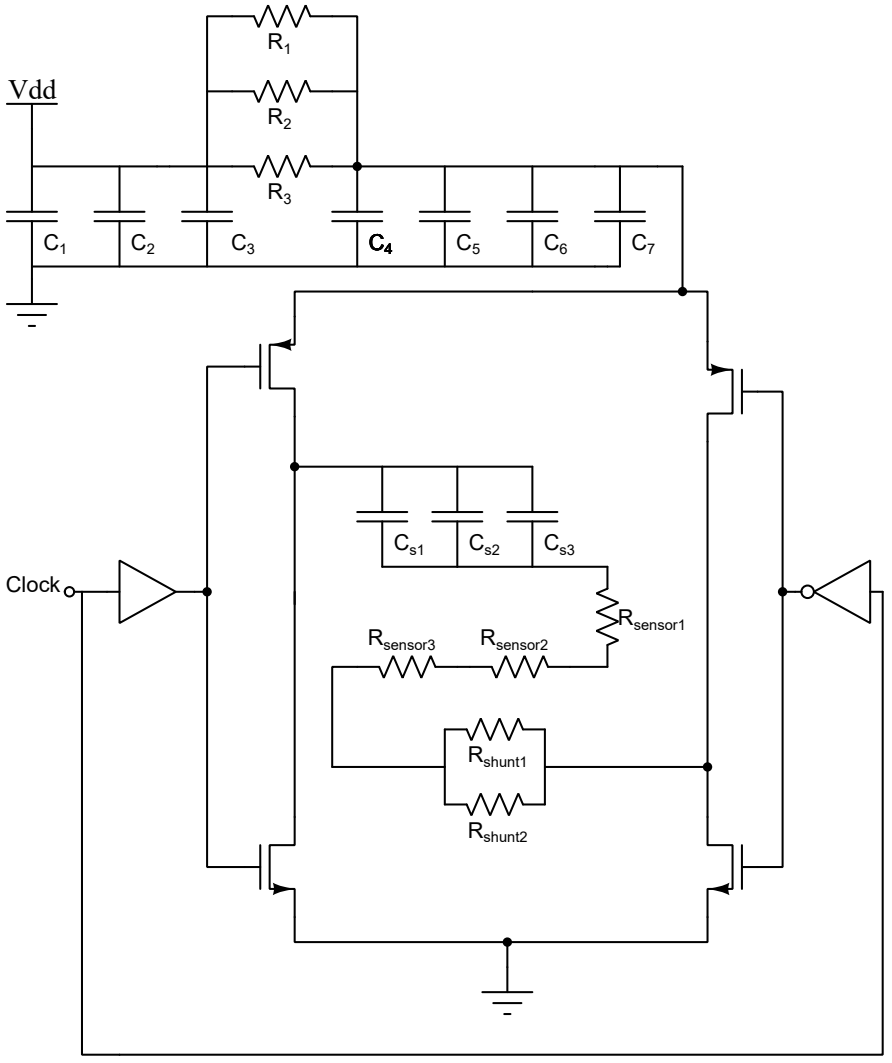

Figure 3.12: MAG-SPEL sensor head with current pulse generator

The current peaks need to be sharp and larger than 4A according to the HMC1001 datasheet. Figure 3.13 and 3.14 is the result of a simulation showing a sharp peak over 4A for approximately 10μs. The simulation itself does not account for any extra effect generated by the vias or copper paths. A slightly higher peak value is expected.

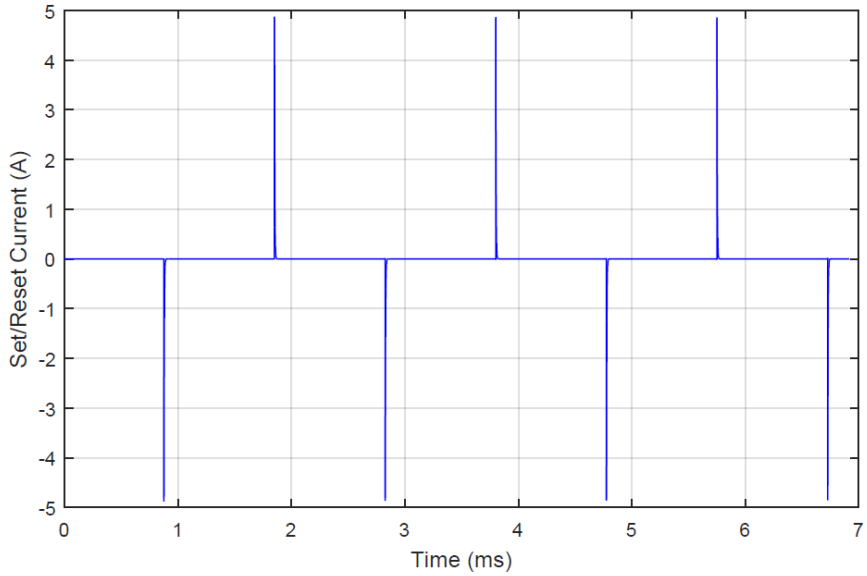

Figure 3.13: SPICE simulation showing the bipolar current pulses

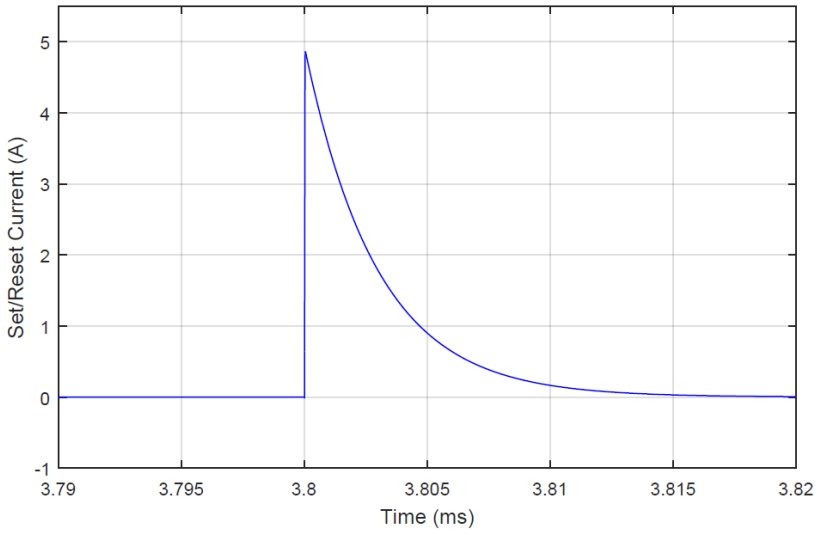

Figure 3.14: Enhanced pulse generated by the previous simulation

3.2 Components selection

The key difference of this type of magnetometers, in contrast with the high-end missions, is the use of only COTS components. The mission has to taken into account that a large high end magnetometer is not possible for the SUCHAI 2/3 mission due to size, power and budget restriction. Therefore all the electronics used must be available commercially. A small research was conducted to find the best suited components for the task. This was done having in mind three key factors: the lowest noise density spectrum possible for reducing noise, the smallest offset voltage so that the integrator can work without problems, and the max output current for the feedback loop. One OPAMP was chosen for MAG-SPEL, and was compared with the OP484 already used by MAGIC. SPICE models where found for each component and simulation where carried out for noise and offset voltage, total integrated noise on the band of 1mHz - 100Khz and offset voltages when configured as a voltage follower.

Table 3.1: Comparative values for two different OPAMPs to be selected for MAG-SPEL

OPAMP	Offset Voltage	NDS at 1KHz	Max output current
OP484	65 μV, 165 μV MAX	3.9 $\frac{nV}{\sqrt{Hz}}$	$\pm$ 6.5mA
ISL28134	0.2 μV, 2.5 μV MAX	10 $\frac{nV}{\sqrt{Hz}}$	$\pm$ 65mA

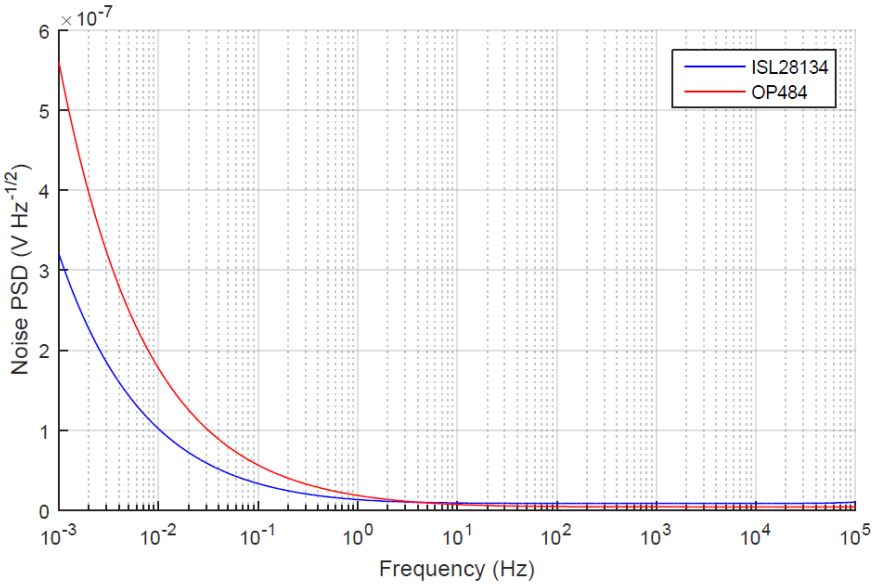

Figure 3.15: Different OPAMP noise density spectrum for the SUCHAI 2/3 component selection

It can be seen that the selected OPAMP by MAGIC does have a small noise density at 1KHz compared to ISL28134, but this frequency is far over the desire frequency of operation of 1mHz to 512Hz. A key factor for deciding is that the ISL28134 has a smaller integrated noise in the band of interest, thus assuring a smaller noise in important sectors of the spectrum.

Table 3.2: Noise and input characteristic of selected OPAMPs.

OPAMP	**Total integrated noise**	**Input Offset Voltage**
OP484	1.2337 μV,	19.7887 μV
ISL28134	2.7608 μV	-238.4 nV

Also the fact that the flicker noise step is smaller than the one presented in the OP484 model simulations works in favor of ISl28134. In terms of the output current, ISL24134 has 10 times more maximum output current than the OP484, which is important when considering the necessary current for the feedback coil and the close loop operation. With all things considered, ISL24138 was chosen for the MAG-SPEL. The rest of the components were chosen considering mostly noise characteristic and rail to rail operation:

- Fully Differential Amplifier: ADA4940
- Instrumentation Amplifier: AD8226
- Switch DPST: TS5A22362
- MOSFET driver: TC4425
- MOSFET: IRF7317

Chapter 4

Results and discussion

4.1 Implementation

MAG-SPEL construction had to consider several factors in order to emulate the final application. The most important ones being:

1. It has to be modular for easy replacement
2. It has to simulate partially the distances and restrictions of a CubeSat
3. It has to be able to function without any human interaction after start up

As such, MAG-SPEL was design in separated PCBs. One was related entirely to the sensor head (HMC1001) and the current generator circuit, and another dedicated to signal processing, power management, and control. This gives the opportunity to test and manage each PCB separately for a smoother transition to a whole system testing.

The sensor head was design to be small as possible, considering that it will be installed in a boom stick deployed out of the SUCHAI 2/3 satellites. It was important to be able to pack all the components for the current generator circuit as close to the magnetic sensors as possible, but also supplying with enough connectors to be able to reach the other half of the MAG-SPEL circuit. An example of the 7th version of the PCB design is shown on figure 4.1. This PCB has a final size of 16 cm^2, having most of its space occupied by the Molex connectors selected for the job due to their robustness and easy connections/disconnection. This secures that in the future the sensor head itself will be half this size, or smaller. All PCBs were constructed by an external vendor.

The components related to the sensor head are the HMC1001 as a magnetic sensor, TC4425 as a double MOSFET driver with both inverted and non-inverted outputs, and a double channel IRF7317 MOSFET for the current generator. Both the driver and the MOSFET are very fragile to human touch and have a tendency to malfunction if touch with bare or non-grounded hands. A single isolated DC-DC converter ITX0515SA with 400 mA maximum output current was used to step up the $5V$ supply voltage to $15V$ in order for the current pulse generator to work accordingly. Only standard voltage rails are available for the SUCHAI 2/3,

which means only $3.3V$ and $5V$ with a $5A$ maximum current. As such, the sensor itself had to generate any other voltage needed for functioning properly. The existence of the DC-DC converter will increase consumption at the cost of being modular and easily implemented.

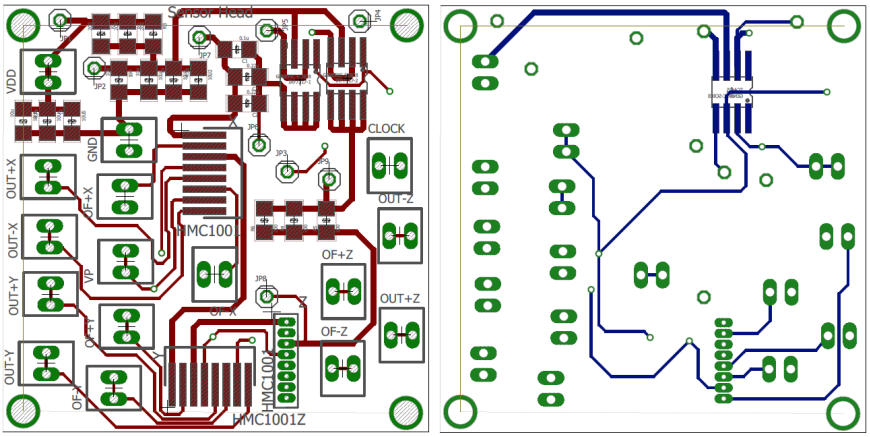

Figure 4.1: PCB CAD for the sensor head of MAG-SPEL

The final result for the sensor head can be seen on figure 4.2.

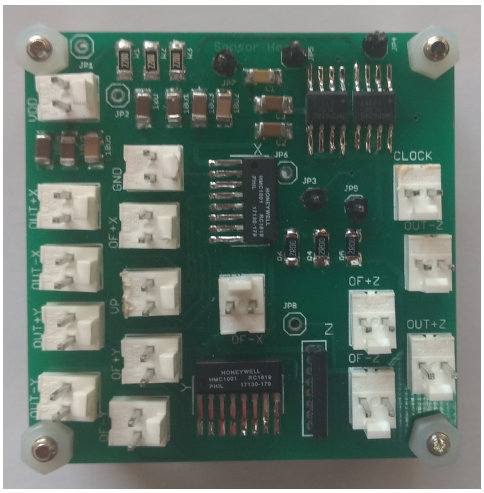

Figure 4.2: Constructed PCB for the sensor head of MAG-SPEL

The signal processing PCB design followed the exact same philosophy as the previous one, with the exception that three different PCB were constructed for each sensor head. As stated, the OPAMP used for the integrators and the feedback were selected due to its noise characteristics and input offset voltage. The same way as the sensor head, the PCB has a 16 cm^2 size that can be reduced when eliminating the big connectors. For the connection between each circuit, 60 cm cables were used to simulated the larges distances possible to obtain in a CubeSat, which is the worst-case scenario for the signal to travel.

The final result for the sensor head can be seen on figure 4.4.

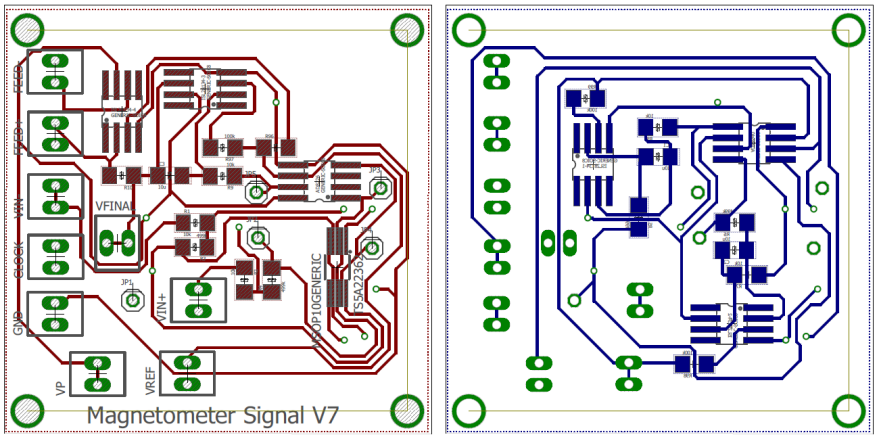

Figure 4.3: PCB CAD for the signal processing of MAG-SPEL

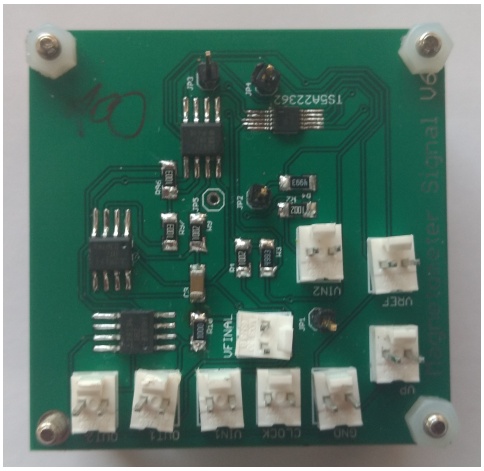

Figure 4.4: Constructed PCB for the signal processing of MAG-SPEL

4.2 Testing

The next step in the development of MAG-SPEL was calibrating and testing the sensor in a controlled environment. There are several ways to do a calibration, such as using a magnetic isolated box with an electromagnet inside to control stimulation or cross calibration with another magnetometer already calibrated or the use of an equipment capable of controlling the ambient magnetic field, like a Helmholtz Cage (HC).

For MAG-SPEL, a Helmholtz Cage was the most straight forward mean of calibration. For such purpose, a trip to Boston University in Boston, MA, USA, was conducted to use their Helmholtz Cage. The test facility was designed and commercialized by Billingsley Aerospace & Defense. I consist of:

- Axial alignment with orthogonality better than $\pm 0.1^0$
- Magnetic constant of 1 Gauss/AMP Nominal
- A calibration accuracy of $\pm 0.015\%$ at Coil Center
- Field Uniformity with a $< 0.3\%$ gradient in a centrally located 20cm sphere and a $<$

0.1% gradient in a centrally located 10 cm sphere

- With a geometry of 3 nested rectangular coil pairs
- Dimension of each coil is 120 cm squared
- Weight 50 kg
- Constructed with all non-magnetic materials; coils are electrically isolated.

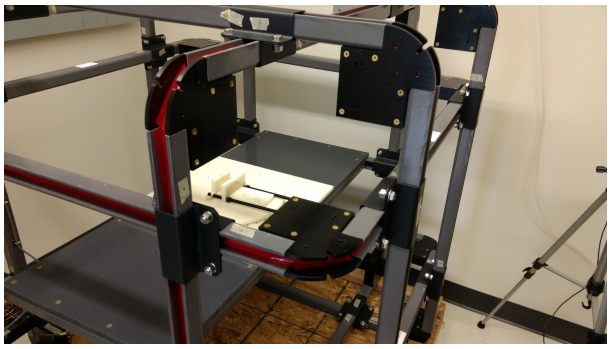

Figure 4.5: Three axis Helmholtz Cage

This HC was available through January 2017 to March 2017 for MAG-SPEL calibration. A second magnetometer, a Bartington three-axial flux gate was also used for cross calibration with the following characteristics:

- Serial Mag-13MSL100
- Noise levels down to $<$ 4pTrms/$sqrtHz$ at 1Hz
- Electrical shielding and IP67 rating on land packaged versions
- Frequency response from DC to 3kHz (-3dB)
- Integrated test coil and temperature sensor
- Typical application: Reference magnetometer for calibration purpose

Figure 4.6: Bartington three axis flux gate magnetometer

With such equipment, a calibration process was designed. A resistor of 100Ω was used as a feedback loop to ensure a large dynamic range of operation and correct range parameters for the feedback OPAMP. This parameter was obtained after trial and error and comparing it to previous iterations using the HMC1001 by Imperial College. All tests were conducted using the full sensor functioning independently from human intervention, including the generation

of the clock (490Hz) and current pulses. The data was collected using a 16 bit NI DAQ provided by Boston University monitored in real time by a PC data logger.

The calibration process was as it follows:

1. Preparing the HC for measurements
   (a) Degaussing the cage
   (b) Calibrating the 0 nT mark at the center of the cage
   (c) Setting each axis to 0 nT at the center of the cage
2. Placing the MAG-SPEL sensor inside de cage directly in the middle point where the previous 0 nT mark was set
   (a) The MAG-SPEL was place inside with: sensor head, signal processing circuit, power supply PCB, Arduino Mega for 490 Hz clock, DAQ and oscilloscope probes
3. The magnetic field is then change from ranges of $\pm$ 60.000 nT with a 5.000 nT step
   (a) Each step was conducted by turning the sensor fully off, setting the new ambient magnetic field, and then turning on the sensor to the ambient magnetic field.
   (b) Sample frequencies were 100 Hz, 1 kHz and 10 kHz for the purpose of future decimation of the signal
4. Before turning the sensor in a 180^0 angle, the Bartington Fluxgate was placed to obtain a cross calibration of exactly the same values collected before
5. The process is then repeated with the sensor flipped 180^0 for a new set of data

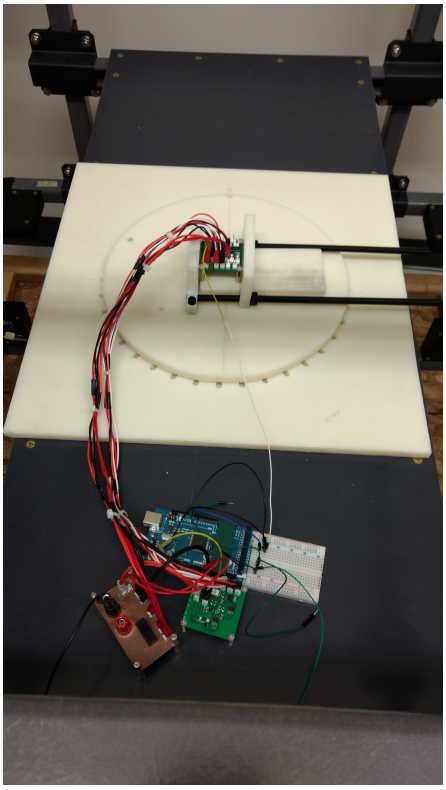

Figure 4.7: MAG-SPEL inside the Helmholtz Cage

4.3 Final results

For each of the steps shown above, a graph is obtained like the one shown on figure 4.8. From 0 s to approximately 4 s the sensor is off. The loading stage occurs due to the time needed for the integrators to set the DC value to the desire point before the data can be correctly interpreted.

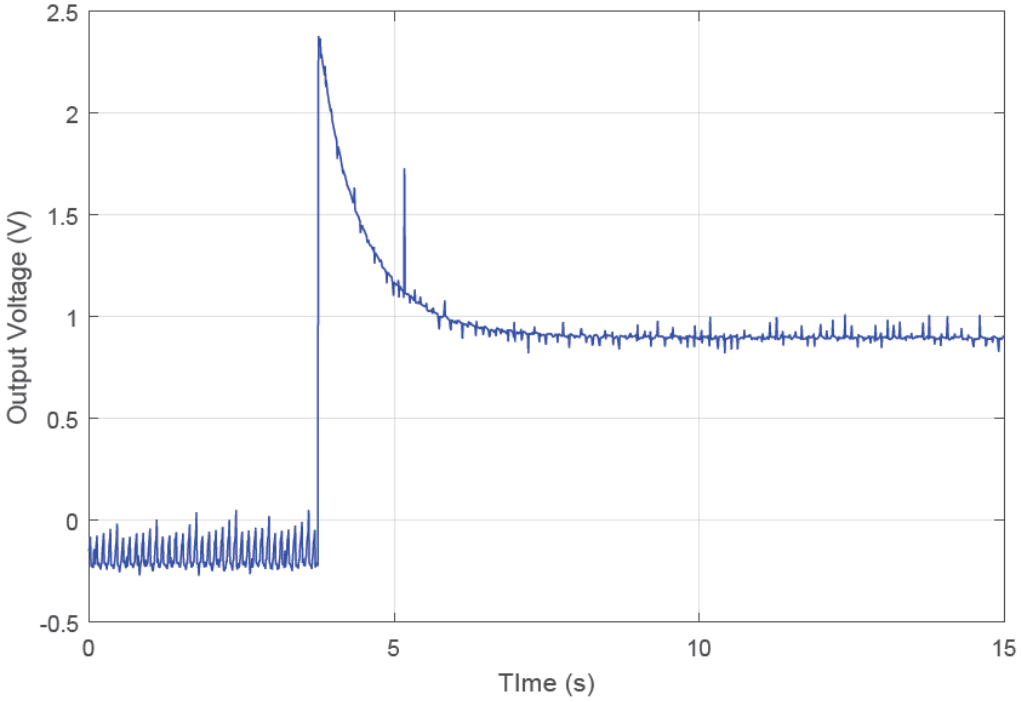

Figure 4.8: Output voltage of MAG-SPEL for a given ambient magnetic field

After the settling time the amplitude of the output voltage (references to V_{bias}) is proportional to the ambient magnetic field. Full functionality is achieved when both the sensor head with the current pulses, and the demodulation stage work in synchrony. In total, 63 different graphs were obtained for each run of MAG-SPEL. Also, data from the reference flux gate magnetometer was saved in order to cross calibrate.

Between each measurement, the current moving through the set/reset straps was also obtained for the purpose of analyzing the correct saturation of the sensor. Figure 4.9 shows how the current pulses generated exceed the simulated value by a 500$[mA]$ margin. This is likely an inductive effect not considered on the initial simulations. As shown, both sides of the bipolar signal have the same peak, thus securing a symmetric saturation of the sensor, just like the counter part of MAGIC[17].

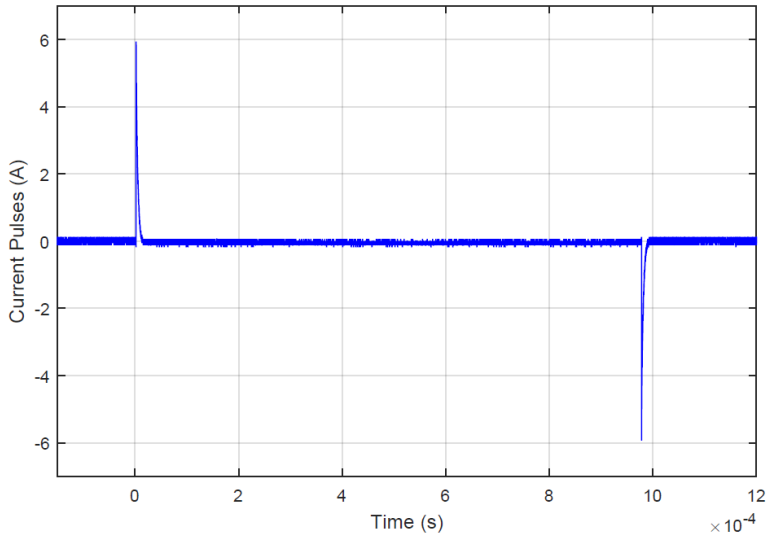

Figure 4.9: Bipolar current pulses obtain from MAG-SPEL testing

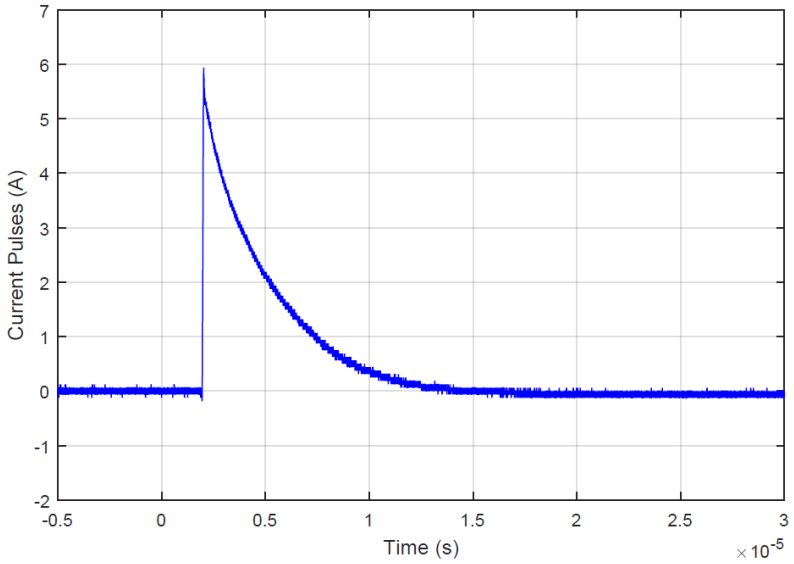

Figure 4.10: Enhanced version of the current pulses from MAG-SPEL

By using all the data from MAG-SPEL and the data from the flux gate cross calibration it is possible to construct a curve relating ambient magnetic field and output voltage of MAG-SPEL. The slope of this curve will be directly related to the value used for the feedback resistor, having a bigger slope with a larger resistor. The value used for the feedback resistor resulted in a dynamic range of $\pm 45.000[nT]$ before the sensor started saturating. Data collected from each iteration confirms a slope or scale factor of $4.8487 \cdot 10^{-5} V/nT$ for transformation purposes, ending with the following equation:

$$BnT = 20383nT/V \cdot V_{output} V \breve{} 53212nT \tag{4.1}$$

Finally, figure 4.11 shows a plot of the collected data. As seen, the saturation occurs around 500 mV from each rail voltage. By testing the sensor without feedback, it was possible to achieve rail-to-rail operation. The 51 $mA/Gauss$ scale factor of the offset strap is small enough for the ISL248134 to reach higher current so to manage larger fields than 45.000 nT.

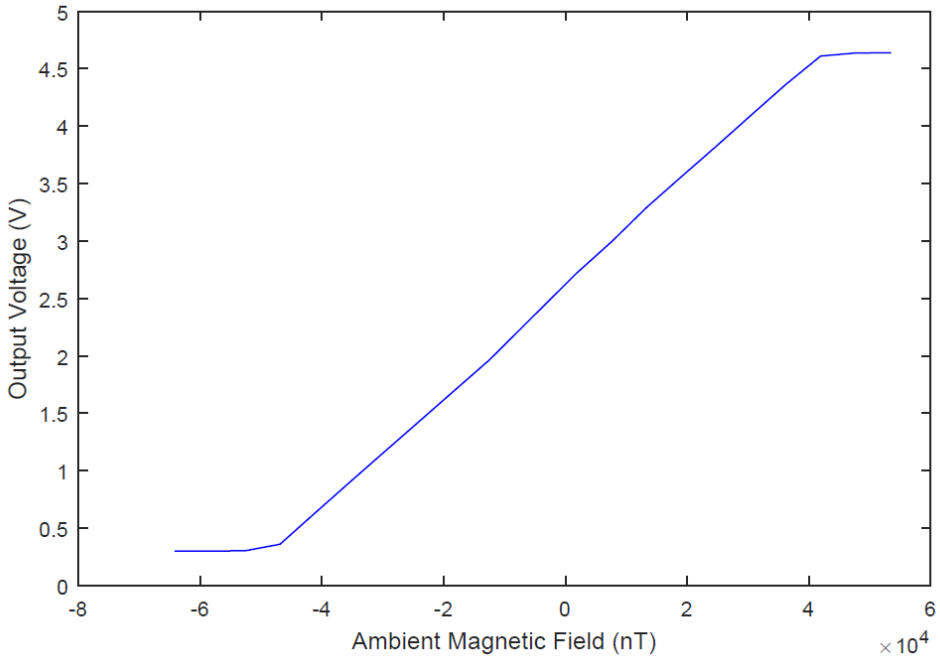

Figure 4.11: Final data relation between ambient magnetic field and output voltage

It is important to notice that the equation is not evenly centered at $0nT = 2.5V$ but rather at $2.610mV$, which indicates an offset not related to the sensor intrinsic offset or reference detector. This can be explained by external currents or fields not properly measured inside the testing facility and other electrical effects not considered in the overall functioning of the sensor.

Different sample rates were used in order to test decimation techniques in noise performance and thus sensitivity. As such, 100Hz, 1khz and 10kHz sample rates were used for experimenting with possible noise reduction. If the noise follows a Gaussian distribution, being a standard white noise, the overall noise should be reduced by decimation. As a result a decrease on read-out noise should be observed as the decimation factor is increased Results for these three frequencies are shown on 4.1

Table 4.1: Instrument Sensitivity

Original sample rate	**Final sensitivity**	**Comment**
100Hz	160-240 nT	no decimation
1kHz	50-90 nT	decimated by 10 samples
10kHz	10-50 nT	decimated by 100 samples

Table 4.2 shows each final characteristic.

Table 4.2: Final parameters of the SUCHAI 2/3 magnetometer MAG-SPEL

Parameter	**Value**	**Comment**
Dynamic range	± 45.000 nT	
Sensitivity	$10 - 50$ nT	Decimated by 100 samples
Scale factor	$4.85 \cdot 10^{-5} \frac{V}{nT}$	
Flipping Frequency	490 Hz	
Power supply	5 V and 0 V	
Power consumption	1.1 W	Three axis operation

By comparing both the table from MAGIC parameters and characteristics from the one from MAG-SPEL, it can be seen that a smaller sensitivity was achieved by MAG-SPEL. This could be part of several factors aimed to reduce noise, from decimation techniques to the fully differential topology used for the initial stages. Although the difference is not as significant as expected, it proves that it is possible to replicate MAGIC and even improve it if more thought is put into the design. Also, it is important to point out the large dynamic range, larger enough for the ambient magnetic field of earth (26.000 nT) and storms that could happen during the SUCHAI 2/3 mission.

The time constant for the sensor to start working and providing data is a drawback when compared with other magnetometers operation, but this can be solved by starting the sensor by stages. During the calibration, all power was taken away from the sensor and given back on each iteration. If power is only cut from the sensor head, it is possible to shorten de waiting period so that it is no detrimental to MAG-SPEL operation.

The power consumed by MAG-SPEL is larger than the one in MAGIC, which can be explained by the DC-DC converter which on its own consumed as much as 300 mW when idle. Better performance can be achieved if the power supply is regulated more delicately. Still, even though the power is larger, it is smaller enough for a CubeSat power system to operate correctly. With a maximum of 4 A operation in SUCHAI 2/3, this payload consumes less than 10% of the full capacity given by the CubeSat, not to mention that this measurement was made in the worst-case scenario of a large ambient magnetic field, thus 1.1 W is the largest power compunction obtained during calibration. Nonetheless, this figure cannot be used as a final value for the payload integration, as a computer and ADC are still missing from the sensor, which will increase power consumption.

The saturation seen on figure 4.11 is not a result components saturation, this is confirmed by using the sensor in an open loop and achieving 5 V and 0 V from the integrator itself. As stated above, the current output of ISL28134 is enough to manage larger magnetic fields. This follow the conclusion that the sensor HMC1001 itself is saturating, which is possible considering all the process that are happening inside it.

As such, it is possible to use MAG-SPEL as a sensor for space physics and for obtaining magnetospheric data with the CubeSat platform. This is because in a calm environment PC-5 have a 40 - 400 nT swings, even if this means than sometimes the sensor will not be

able to obtain a value due to the signal being smaller than the minimum noise level achieved. It is important to consider though that this would be the case in a quiet scenario, which could become thousands of nT in the event of a magnetic storm that are very interesting for the mission. Also, it could be used for navigation or any other less detail measurement.

Chapter 5

Conclusion

The present thesis improves the work regarding AMR magnetometer following the proposed topology and sensor by Imperial College and MAGIC. As such, an informed decision on which type of sensor to use was achieved thanks to the study that allow to comprehend each mainstream magnetic sensor with their advantages, disadvantages, and general application, including space based sensor still working today in space. This decision was also influenced by the knowledge of which type of magnetic event is desire to measure with MAG-SPEL which lead to an initial study of plasma physics and the magnetic pulsations that occur in the magnetosphere and the need of a measurement only at the poles due to the large distance between earth and the actual origin of PC waves. With all this information gathered it was possible to carefully design changes in the topology proposed by MAGIC and build a successful MAG-SPEL.

The simulations carried during the process of understanding the principle of operation of MAGIC gave enough insight so that the change to MAG-SPEL design was fluid and without any problem. In terms of the design of MAG-SPEL it was possible to change several key stages such as demodulation and offset compensation in order to improve performance and reducing the error related to resistors mismatch by using a fully differential scheme, which accompanied by simulations and analytical development was implemented and integrated to the overall design flawlessly. New electronic components were chosen in order to fulfill total close loop operation and during such process noise could also be reduced thank to the smaller flicker noise step of ISL28134, feature not present on the original MAGIC. In terms of power supply, the restriction of only 5 V was overcome by the use of an isolated DC-DC converter that was powerful enough for the current pulses to be as sharp and large as possible as simulations tested.

Thanks to the support of Boston University both a reference magnetometer and a special facility were provided for testing and calibration of MAG-SPEL. For such task, modular PCBs were designed having in mind that it should be easy to interchange pieces and sensor for a swift and easy operation. This led to professionally built PCBs that were assembled at Boston University. At such point, the feedback resistor became an issue which was solve by trial and error thus securing a large dynamic range of approximately $\pm$ 45.000 nT, a value that is over the desire threshold.

A methodology was designed for the testing process, where the reference magnetometer and the Helmholtz cage were used in synergy. It was possible to test the sensor from large to small magnetic field without any human intervention on itself, thus securing an autonomous operation and showing no evidence of problems in terms of stability while functioning. The use of a simple decimation was incredibly helpful in the process, which by understanding that occurs at extremely low frequencies, filters and mathematical tools can be used for an improved sensibility. It was possible to obtain all the important variables of merit such as noise, power consumption and dynamic range of MAG-SPEL which led to 10-50 nT sensitivity, which is an improvement compared to the MAGIC design. It is smaller than the previous MAGIC iteration of the same sensor. Power consumption was keep inside the desire values of operation given by a CubeSat which secures a spot on the SUCHAI 2/3 missions to come.

Finally, it can be said that all the objectives of this theses were met and the hypotheses that a competitive magnetometer could be built, and also improved, using MAGIC from Imperial College as a reference, even if several restrictions from the SUCHAI 2/3 mission are included. It is important to point out that more improvements can be made to MAG-SPEL, especially in the power supply area and current pulse generator, and a PC104 (the CubeSat standard for PCB) can be built with MAG-SPEL to achieve a more realistic calibration.

5.1 Future work

From the work developed several future projects can follow up the MAG-SPEL construction:

- Implementation of the digital stage, including a processor for synchronizing an ADC for data acquisition. Such stage is more related to the integration of the MAG-SPEL into a CubeSat, with posses the problem of coordination with the main bus, computer and transceiver for optimal operation.
- Further development can be achieved in the power supply area by including a more stable and less noise DC-DC and regulators
- The development of a technique in which, by using two or more MAG-SPEL simultaneously, it would be possible to set the 0 nT field somewhere higher. This higher value could be the DC ambient magnetic field obtained by one of the MAG-SPEL sensors. This was, one MAG-SPEL with a small dynamic range but great noise performance and sensitivity can be used to measure the variations of the ambient magnetic field thanks to the reference provided by a different MAG-SPEL with large dynamic range.
- Development of a variation of MAG-SPEL for earth based measurements that could work along with the SAMBA flux gate magnetometer network. This could include the option of higher power available, thus changing parts of MAG-SPEL to use such difference to the sensitivity advantage.
- Development of a simpler version of MAG-SPEL for the purpose of pico-satellite operation.
- The sensor will be tested at NASA Goddard in August for further calibration check.

Bibliography

[1] C. Coillot, J. Moutoussamy, P. Leroy, G. Chanteur, and A. Roux, "Improvements on the design of search coil magnetometer for space experiments," *sensor letters*, vol. 5, no. 1, pp. 167–170, 2007.

[2] P. Ripka, "Fluxgate sensors," in *Magnetic Sensors and Magnetometers*, pp. 75–128, 2001.

[3] F. Primdahl, "The fluxgate mechanism, part i: The gating curves of parallel and orthogonal fluxgates," *IEEE transactions on magnetics*, vol. 6, no. 2, pp. 376–383, 1970.

[4] H. Hauser and M. Tondra, "Magnetoresistors," in *Magnetic Sensors and Magnetometers*, pp. 129–171, 2001.

[5] K. Woellert, P. Ehrenfreund, A. J. Ricco, and H. Hertzfeld, "Cubesats: Cost-effective science and technology platforms for emerging and developing nations," *Advances in Space Research*, vol. 47, no. 4, pp. 663–684, 2011.

[6] M. Diaz, J. Zagal, C. Falcon, M. Stepanova, J. Valdivia, M. Martinez-Ledesma, J. Diaz-Pena, F. Jaramillo, N. Romanova, E. Pacheco, *et al.*, "New opportunities offered by cubesats for space research in latin america: The suchai project case," *Advances in Space Research*, vol. 58, no. 10, pp. 2134–2147, 2016.

[7] H. Auster, K. Glassmeier, W. Magnes, O. Aydogar, W. Baumjohann, D. Constantinescu, D. Fischer, K. Fornacon, E. Georgescu, P. Harvey, *et al.*, "The themis fluxgate magnetometer," in *The THEMIS Mission*, pp. 235–264, Springer, 2009.

[8] M. H. Acuna, "Space-based magnetometers," *Review of scientific instruments*, vol. 73, no. 11, pp. 3717–3736, 2002.

[9] M. Díaz-Michelena, "Small magnetic sensors for space applications," *Sensors*, vol. 9, no. 4, pp. 2271–2288, 2009.

[10] M. H. Acuna and C. J. Pellerin, "A miniature two-axis fluxgate magnetometer," *Geoscience Electronics, IEEE Transactions on*, vol. 7, no. 4, pp. 252–260, 1969.

[11] M. H. Acuna, "Fluxgate magnetometers for outer planets exploration," *IEEE Transactions on Magnetics*, vol. MAG-10, pp. 519–523, May 1974.

[12] K.-H. Glassmeier, H.-U. Auster, D. Heyner, K. Okrafka, C. Carr, G. Berghofer, B. An-

derson, A. Balogh, W. Baumjohann, P. Cargill, *et al.*, "The fluxgate magnetometer of the bepicolombo mercury planetary orbiter," *Planetary and Space Science*, vol. 58, no. 1, pp. 287–299, 2010.

[13] W. Magnes, D. Pierce, A. Valavanoglou, J. Means, W. Baumjohann, C. Russell, K. Schwingenschuh, and G. Graber, "A sigma–delta fluxgate magnetometer for space applications," *Measurement Science and Technology*, vol. 14, no. 7, p. 1003, 2003.

[14] E. Matandirotya, R. R. Van Zyl, D. J. Gouws, and E. F. Saunderson, "Evaluation of a commercial-off-the-shelf fluxgate magnetometer for cubesat space magnetometry," 2013.

[15] D. Duret, J. Bonzom, M. Brochier, M. Frances, J. Leger, R. Odru, C. Salvi, T. Thomas, and A. Perret, "Overhauser magnetometer for the danish oersted satellite," *Magnetics, IEEE Transactions on*, vol. 31, no. 6, pp. 3197–3199, 1995.

[16] P. Brown, B. Whiteside, T. Beek, P. Fox, T. Horbury, T. Oddy, M. Archer, J. Eastwood, D. Sanz-Hernández, J. Sample, *et al.*, "Space magnetometer based on an anisotropic magnetoresistive hybrid sensor," *Review of Scientific Instruments*, vol. 85, no. 12, p. 125117, 2014.

[17] P. Brown, T. Beek, C. Carr, H. O'Brien, E. Cupido, T. Oddy, and T. Horbury, "Magnetoresistive magnetometer for space science applications," *Measurement Science and Technology*, vol. 23, no. 2, p. 025902, 2012.

[18] S. R. Burr, *The design and implementation of the Dynamic Ionosphere Cubesat Experiment (DICE) science instruments*. PhD thesis, Citeseer, 2013.

[19] J. Lenz and A. S. Edelstein, "Magnetic sensors and their applications," *Sensors Journal, IEEE*, vol. 6, no. 3, pp. 631–649, 2006.

[20] M. J. Caruso, T. Bratland, C. H. Smith, and R. Schneider, "A new perspective on magnetic field sensing," *SENSORS-PETERBOROUGH-*, vol. 15, pp. 34–47, 1998.

[21] T. Q. Yang and K. Enpuku, "Squid magnetometer utilizing normal pickup coil and resonant-type coupling circuit," *Physica C: Superconductivity*, vol. 392, pp. 1396–1400, 2003.

[22] V. Pizzella, S. Della Penna, C. Del Gratta, and G. L. Romani, "Squid systems for biomagnetic imaging," *Superconductor Science and Technology*, vol. 14, no. 7, p. R79, 2001.

[23] H.-G. Meyer, R. Stolz, A. Chwala, and M. Schulz, "Squid technology for geophysical exploration," *physica status solidi (c)*, vol. 2, no. 5, pp. 1504–1509, 2005.

[24] J. Moutoussamy, C. Coillot, G. Chanteur, and F. Alves, "Feasibility of a giant magnetoimpedance sandwich magnetometer for space applications," in *Sensors, 2007 IEEE*, pp. 1013–1016, IEEE, 2007.

[25] P. Ripka, "Induction sensors," in *Magnetic Sensors and Magnetometers*, pp. 47–74, 2001.

[26] V. F. Labson, A. Becker, H. Morrison, and U. Conti, "Geophysical exploration with audiofrequency natural magnetic fields," *Geophysics*, vol. 50, no. 4, pp. 656–664, 1985.

[27] S. A. Macintyre, "Magnetic field sensor design," *Sensor Review*, vol. 11, no. 2, pp. 7–11, 1991.

[28] P. Kašpar and P. Ripka, "Induction coils: voltage versus current output," in *Imeko World Congress*, pp. 55–60, 2000.

[29] A. Roux, O. Le Contel, C. Coillot, A. Bouabdellah, B. De La Porte, D. Alison, S. Ruocco, and M.-C. Vassal, "The search coil magnetometer for themis," in *The THEMIS Mission*, pp. 265–275, Springer, 2009.

[30] W. Stuart, "Earth's field magnetometry," *Reports on Progress in Physics*, vol. 35, no. 2, p. 803, 1972.

[31] G. Dehmel, "Induction sensors," *Magnetic sensors*, pp. 205–255, 1989.

[32] M. Parrot, D. Benoist, J. Berthelier, J. Błecki, Y. Chapuis, F. Colin, F. Elie, P. Fergeau, D. Lagoutte, F. Lefeuvre, *et al.*, "The magnetic field experiment imsc and its data processing onboard demeter: Scientific objectives, description and first results," *Planetary and Space Science*, vol. 54, no. 5, pp. 441–455, 2006.

[33] H. Seran and P. Fergeau, "An optimized low-frequency three-axis search coil magnetometer for space research," *Review of scientific instruments*, vol. 76, no. 4, p. 044502, 2005.

[34] A. Grosz, E. Paperno, S. Amrusi, and B. Zadov, "A three-axial search coil magnetometer optimized for small size, low power, and low frequencies," *Sensors Journal, IEEE*, vol. 11, no. 4, pp. 1088–1094, 2011.

[35] P. Ripka, F. Primdahl, O. V. Nielsen, J. R. Petersen, and A. Ranta, "Ac magnetic-field measurement using the fluxgate," *Sensors and Actuators A: Physical*, vol. 46, no. 1, pp. 307–311, 1995.

[36] T. Sonoda and R. Ueda, "Distinctive features of magnetic field controlled type magnetic field sensor," *IEEE Transactions on Magnetics*, vol. 25, no. 5, pp. 3393–3395, 1989.

[37] A. R. of Moldovanu, H. Chiriac, M. Macoviciuc, E. Diaconu, C. Ioan, E. R. of Moldovanu, and M. Tomut, "1st european magnetic sensors and actuators conference functional study of fluxgate sensors with amorphous magnetic materials cores," *Sensors and Actuators A: Physical*, vol. 59, no. 1, pp. 105 – 108, 1997.

[38] J. R. Burger, "The theoretical output of a ring core fluxgate sensor," *Magnetics, IEEE Transactions on*, vol. 8, no. 4, pp. 791–796, 1972.

[39] W. Thomson, "On the electro-dynamic qualities of metals:–effects of magnetization on the electric conductivity of nickel and of iron," *Proceedings of the Royal Society of London*, vol. 8, pp. 546–550, 1856.

[40] M. N. Baibich, J. M. Broto, A. Fert, F. N. Van Dau, F. Petroff, P. Etienne, G. Creuzet, A. Friederich, and J. Chazelas, "Giant magnetoresistance of (001) fe/(001) cr magnetic superlattices," *Physical review letters*, vol. 61, no. 21, p. 2472, 1988.

[41] J. L. Brown, "High sensitivity magnetic field sensor using gmr materials with integrated electronics," in *Circuits and Systems, 1995. ISCAS'95., 1995 IEEE International Symposium on*, vol. 3, pp. 1864–1867, IEEE, 1995.

[42] P. Freitas, F. Silva, N. Oliveira, L. Melo, L. Costa, and N. Almeida, "Spin valve sensors," *Sensors and Actuators A: Physical*, vol. 81, no. 1, pp. 2–8, 2000.

[43] J. Daughton, J. Brown, E. Chen, R. Beech, A. Pohm, and W. Kude, "Magnetic field sensors using gmr multilayer," *Magnetics, IEEE Transactions on*, vol. 30, no. 6, pp. 4608–4610, 1994.

[44] J. Rife, M. Miller, P. Sheehan, C. Tamanaha, M. Tondra, and L. Whitman, "Design and performance of gmr sensors for the detection of magnetic microbeads in biosensors," *Sensors and Actuators A: Physical*, vol. 107, no. 3, pp. 209–218, 2003.

[45] T. McGuire and R. Potter, "Anisotropic magnetoresistance in ferromagnetic 3d alloys," *IEEE Transactions on Magnetics*, vol. 11, no. 4, pp. 1018–1038, 1975.

[46] L.-Y. Liu, S.-B. Jiang, T.-L. Yeh, H.-C. Yeh, J.-Y. Liu, Y.-H. Hsu, and J.-Y. Peng, "The magneto-resistive magnetometer of bcu on the tatiana-2 satellite," *Terrestrial, Atmospheric and Oceanic Sciences*, vol. 23, no. 3, pp. 317–326, 2012.

[47] S. Leitner, A. Valavanoglou, P. Brown, C. Hagen, W. Magnes, B. J. Whiteside, C. M. Carr, M. Delva, and W. Baumjohann, "Design of the magnetoresistive magnetometer for esa's sosmag project," *IEEE Transactions on Magnetics*, vol. 51, no. 1, pp. 1–4, 2015.

[48] Honywell, "1 and 2 axis magnetic sensors hmc1001/hmc1002/hmc1021/hmc1022," tech. rep., Honywell, Aug. 2008.

[49] H. Hauser, P. L. Fulmek, P. Haumer, M. Vopalensky, and P. Ripka, "Flipping field and stability in anisotropic magnetoresistive sensors," *Sensors and Actuators A: Physical*, vol. 106, no. 1, pp. 121–125, 2003.

[50] M. Endoh, N. Shimizu, H. Yoda, and N. Waoatsuki, "Highly sensitive thin film magnetoresistive sensor with good linearity," in *Electronic Manufacturing Technology Symposium, 1988, Design-to-Manufacturing Transfer Cycle. Fifth IEEE/CHMT International*, pp. 210–214, IEEE, 1988.

[51] S. Tumanski, "A new type of thin film magnetoresistive magnetometer–an analysis of circuit principles," *Magnetics, IEEE Transactions on*, vol. 20, no. 5, pp. 1720–1722, 1984.

[52] J. Dungey, "Hydromagnetic waves, physics of geomagnetic phenomena s," *Matsushita, WH Campbell*, vol. 913, 1967.

[53] D. A. Gurnett and A. Bhattacharjee, "Introduction to plasma physics," *Press Syndicate of the University of Cambridge, Cambridge*, p. 9, 2005.

[54] B. Anderson, "An overview of spacecraft observations of 10 s to 600 s period magnetic pulsations in the earth's magnetosphere," *Solar wind sources of magnetospheric Ultra-Low-Frequency waves*, pp. 25–43, 1994.

[55] K. Melikyan, V. Pilipenko, and O. Kozyreva, "Spatial structure of pc5 waves in the outer magnetosphere according to observations onboard the themis satellites," *Cosmic Research*, vol. 51, no. 3, pp. 165–176, 2013.

[56] H. Schmid, "Aaargh! i just loooove flicker noise [open column]," *Circuits and Systems Magazine, IEEE*, vol. 7, no. 1, pp. 32–35, 2007.

[57] N. A. Stutzke, S. E. Russek, D. P. Pappas, and M. Tondra, "Low-frequency noise measurements on commercial magnetoresistive magnetic field sensors," *Journal of Applied Physics*, vol. 97, no. 10, p. 10Q107, 2005.

[58] P. Nandi, D. Sahu, A. S. Dhar, and S. Das, "Spice compatible behavioural modelling of resistive sensors," *Measurement Science and Technology*, vol. 25, no. 5, p. 055104, 2014.

[59] R. D. Middlebrook, "Measurement of loop gain in feedback systems," *International Journal of Electronics Theoretical and Experimental*, vol. 38, no. 4, pp. 485–512, 1975.

[60] R. D. Middlebrook, "The general feedback theorem: a final solution for feedback systems," *IEEE microwave magazine*, vol. 7, no. 2, pp. 50–63, 2006.

Chapter 6

Appendix A: MHD development

6.1 Basic MHD Equations

The equations usually used in MHD come from the momentum and continuity equations of mass seen in kinetic theory, where moment zero, which is simply an equation of continuity for each species " s ", has the following form:

$$\frac{\partial n_s}{\partial t} + \vec{\nabla} \cdot (n_s \vec{U}_s) = 0 \tag{6.1}$$

Where n_s represents the particle density of the species s and $\vec{U}_s$ is the average velocity of the particles of the species s

Thus, the first moment, which is named equation of momentum, has the following initial form:

$$\frac{\partial}{\partial t}(m_s n_s \vec{U}_s) + \vec{\nabla} \cdot (m_s n_s \vec{U}_s \vec{U}_s) = n_s \mathrm{e}_s(\vec{E} + \vec{U}_s \times \vec{B}) - \nabla \cdot \bar{P}_s + \frac{\delta \vec{p}_s}{\delta t} \tag{6.2}$$

Where: m_s is the mass of the species s, e_s is the charge of the species s, $\vec{B}$ represents the magnetic field, $\bar{P}_s$ is the pressure tensor of each species. Finally $\frac{\delta \vec{p}_s}{\delta t}$ is the average change in momentum per unit volume given the collisions. In a simpler way:

$$m_s n_s \frac{\mathrm{d}\vec{U}_s}{t} = n_s \mathrm{e}_s[\vec{E} + \vec{U}_s \times \vec{B}] - \nabla \cdot \bar{P}_s + \frac{\delta \vec{p}_s}{\delta t} \tag{6.3}$$

The presentation of both equations will help to calculate the equations of MHD

Finally, the third moment, called energy equation, has the following form:

$$\frac{\partial W_s}{\partial t} + \vec{\nabla} \cdot \vec{Q}_s - \vec{E} \cdot \vec{J}_s = \int_V \frac{1}{2} m_s v^2 \frac{\delta \vec{p}_s}{\delta t} \mathrm{d}^3 v \tag{6.4}$$

Thus, for the derivation of the MHD equations, it is convenient to define a new mass density equal to the sum of the mass densities of each species individually:

$$\rho_m = \sum_s \rho_{ms} \tag{6.5}$$

Where: $\rho_{ms} = m_s n_s$. Fluid velocity is also defined as the mass-weighted velocity of different species of particles:

$$\vec{U} = \frac{1}{\rho_m} \sum_s \rho_{ms} \vec{U}_s \tag{6.6}$$

6.1.1 Mass Continuity Equation

The mass continuity equation of the species s is:

$$\frac{\partial \rho_{ms}}{\partial t} + \vec{\nabla} \cdot (\rho_{ms} \vec{U}_s) = 0 \tag{6.7}$$

This is obtained by multiplying (6.1) by m_s and using the definition of $\rho_{ms} = m_s n_s$. In addition, adding on all species results in:

$$\frac{\partial \rho_m}{\partial t} + \vec{\nabla} \cdot (\rho_m \vec{U}) = 0 \tag{6.8}$$

Known as the mass continuity equation in fluid dynamics. It is important to note the difference where the velocity of the fluid ends up being masses weighted by the speeds of different species. Not a simple sum.

6.1.2 Momentum equation

Equation of momentum To obtain an equation giving a temporal variation of the moment, we start with the equation (6.2) to take it to the field of fluids. To divide, it is summed on all the species obtaining:

$$\sum_s \frac{\partial}{\partial t}(\rho_{ms}\vec{U}_s) + \sum_s \vec{\nabla}\cdot(\rho_{ms}\vec{U}_s\vec{U}_s) = p_q\vec{E} + \vec{J}\times\vec{B} - \vec{\nabla}\cdot\left(\sum_s \bar{P}_s\right) + \sum_s \frac{\delta\vec{p}_s}{\delta t} \tag{6.9}$$

Where $p_q = \sum_s n_s \mathrm{e}_s$ and $\vec{J} = \sum_s n_s \mathrm{e}_s \vec{U}_s$ has been used. Since the total momentum is conserved for any collision process, $\sum_s \frac{\delta\vec{p}_s}{\delta t}$ must add zero. In addition, it is useful to define a new pressure tensor that moves in the fluid reference frame:

$$\bar{P}_{0s} = m_s \int_{-\infty}^{\infty} (\vec{v}-\vec{U})(\vec{v}-\vec{U}) f_s \mathrm{d}^3 v \tag{6.10}$$

It can be shown that:

$$\bar{P}_{0s} = \bar{P}_s + \rho_{ms}\vec{W}_s\vec{W}_s \tag{6.11}$$

Where $\vec{W}_s = \vec{U}_s - \vec{U}$ Is the average speed of the species s with respect to the velocity of the fluid. Thus, the equation of momentum becomes:

$$\sum_s \frac{\partial}{\partial t}(\rho_{ms}\vec{U}_s) + \sum_s \vec{\nabla}\cdot(\rho_{ms}\vec{U}_s\vec{U}_s) = p_q\vec{E} + \vec{J}\times\vec{B} - \vec{\nabla}\cdot\bar{P}_0 + \sum_s \vec{\nabla}\cdot(\rho_{ms}\vec{W}_s\vec{W}_s) \tag{6.12}$$

Now, replacing $\vec{U}_s = \vec{W}_s + \vec{U}$, the left side of the equation (6.2) takes the following form:

$$\frac{\partial}{\partial t}(\rho_{ms}\vec{U}) + \frac{\partial}{\partial t}(\rho_{ms}\vec{W}_s) + \vec{\nabla}\cdot(\rho_{ms}\vec{W}_s\vec{W}_s) + \vec{\nabla}\cdot(\rho_{ms}\vec{W}_s\vec{U}) + \vec{\nabla}\cdot(\rho_{ms}\vec{U}\vec{W}_s) + \vec{\nabla}\cdot(\rho_{ms}\vec{U}\vec{U}) \tag{6.13}$$

Now, adding over all species, and taking into account that $\sum_s \vec{W}_s\rho_s = 0$ given the nature of the definition of $\vec{W}_s$ is simplified in:

$$\sum_s \frac{\partial}{\partial t}(\rho_{ms}\vec{U}) + \sum_s \vec{\nabla}\cdot(\rho_{ms}\vec{U}\vec{U}) + \vec{\nabla}\cdot(\rho_{ms}\vec{W}_s\vec{W}_s) \tag{6.14}$$

Substituting on the left side of 6.12:

$$\frac{\partial}{\partial t}(\rho_m \vec{U}) + \vec{\nabla} \cdot (\rho_{ms} \vec{U}\vec{U}) = p_q \vec{E} + \vec{J} \times \vec{B} - \vec{\nabla} \cdot \bar{P}_0 \tag{6.15}$$

What is further simplified using the continuity equation:

$$\rho_m \left[\frac{\partial \vec{U}}{\partial t} + (\vec{U} \cdot \vec{\nabla})\vec{U} \right] = p_q \vec{E} + \vec{J} \times \vec{B} - \vec{\nabla} \cdot \bar{P}_0 \tag{6.16}$$

Where the left side is nothing more than the convective derivative, $\mathrm{d}\vec{U}/\mathrm{d}t$. This is the momentum equation, which carries the interpretation that moment changes in a fluid are due to the sum of the electric field, magnetic field and pressure forces.

6.1.3 Generalized ohm law

It is important to always consider that we are before magnetic, electric, and plasma fields in motion. Thus, the general equation of ohm has the following form:

$$\vec{J} = \sigma(\vec{E} + \vec{U} \times \vec{B}) \tag{6.17}$$

6.1.4 Final set of equations

To arrive at this some assumptions must be made:

1. The temporal variations are assumed to be slow, so the displacement current is ignored in comparison to the driving current.
2. It is assumed that the plasma is neutral, so $p_q = 0$.

$$\vec{\nabla} \times \vec{B} = \mu_0 \vec{J} \qquad \text{Ampére's law} \tag{6.18}$$

$$\vec{\nabla} \cdot \vec{B} = 0 \tag{6.19}$$

$$\vec{\nabla} \times \vec{E} = -\frac{\partial \vec{B}}{\partial t} \qquad \text{Faraday's Law} \tag{6.20}$$

$$\vec{\nabla} \cdot \vec{E} = 0 \qquad \text{Gauss' law} \tag{6.21}$$

$$\frac{\partial \rho_m}{\partial t} + \vec{\nabla} \cdot (\rho_m \vec{U}) = 0 \qquad \text{mass continuity equation} \tag{6.22}$$

$$\rho_m \frac{\mathrm{d}\vec{U}}{\mathrm{d}t} = \vec{J} \times \vec{B} - \vec{\nabla} \cdot \bar{P}_0 \qquad \text{momentum equation} \tag{6.23}$$

$$\vec{J} = \sigma(\vec{E} + \vec{U} \times \vec{B}) \qquad \text{Ohm's law} \tag{6.24}$$

$$\frac{\mathrm{d}}{\mathrm{d}t}(P \rho_m^{-\gamma}) = 0 \qquad \text{equation of state} \tag{6.25}$$

6.2 MHD waves

It is important and interesting to consider the propagation of small amplitude waves through a homogeneous and ideal plasma. To linearize these equations, we consider that $\vec{U}$, ρ_m, $\vec{B}$ and P are the sum of variables spatially uniform and independent of time in order zero plus a disturbance in the first order. Thus, it is interesting to obtain the dispersion relations of these waves.

$$\vec{U} = \vec{U}_0 + \vec{U}_1 \tag{6.26}$$

$$\vec{B} = \vec{B}_0 + \vec{B}_1 \tag{6.27}$$

$$\rho_m = \rho_{m0} + \rho_{m1} \tag{6.28}$$

$$P = P_0 + P_1 \tag{6.29}$$

Thus, the first-order linearization of the equations to be used are:

$$\frac{\partial \rho_{m1}}{\partial t} + \rho_{m0} \vec{\nabla} \cdot \vec{U}_1 = 0 \tag{6.30}$$

$$\rho_{m0} \frac{\mathrm{d}\vec{U}_1}{\mathrm{d}t} = \frac{1}{\mu_0} (\vec{\nabla} \times \vec{B}_1) \times \vec{B}_0 - \vec{\nabla} \cdot \bar{P}_1 \tag{6.31}$$

$$\frac{\partial \vec{B}_1}{\partial t} = \vec{\nabla} \times (\vec{U}_1 \times \vec{B}_0) \tag{6.32}$$

$$P_1 = \gamma \left[\frac{P_0}{\rho_{m0}} \right] \rho_{m1} \tag{6.33}$$

To continue, it is appropriate to define the speed of sound V_s:

$$V_s^2 = \gamma \frac{P_0}{\rho_{m0}} \tag{6.34}$$

Next, it is interesting to analyze the equations already shown in the fourier space, where $\vec{\nabla} = \mathrm{i}\vec{k}$ and $\partial/\partial t = -\mathrm{i}\omega$

$$-\mathrm{i}\omega\hat{\rho}_m + \mathrm{i}\rho_{m0}\vec{k} \times \hat{\vec{U}} = 0 \tag{6.35}$$

$$-\mathrm{i}\omega\hat{\rho}_m\hat{\vec{U}} = \frac{\mathrm{i}}{\mu_0}(\vec{k} \times \hat{\vec{B}}) \times \vec{B}_0 - \mathrm{i}\vec{k}\hat{P} \tag{6.36}$$

$$-\mathrm{i}\omega\hat{\vec{B}} = \mathrm{i}\vec{k} \times (\hat{\vec{U}} \times \vec{B}_0) \tag{6.37}$$

$$\hat{P} = V_s^2\hat{\rho}_m \tag{6.38}$$

It is possible to eliminate $\hat{\rho}_m$ from 6.38 by using 6.35:

$$\hat{P} = V_s^2\frac{\rho_{m0}}{\omega}\vec{k} \times \hat{\vec{U}} \tag{6.39}$$

The same way it is possible to eliminate $\hat{P}$ from 6.36, and after multiplying it by $\mathrm{i}\omega/\rho_{m0}$:

$$\omega^2\hat{\vec{U}} = \frac{-\omega}{\mu_0\rho_{m0}}(\vec{k} \times \hat{\vec{B}}) \times \vec{B}_0 + V_s^2\vec{k}(\vec{k} \cdot \hat{\vec{U}}) \tag{6.40}$$

Finally $\hat{\vec{B}}$ can be eliminated by using 6.37 which gives a homogeneous equation for the velocity of the fluid:

$$\omega^2\hat{\vec{U}} = \frac{-\omega}{\mu_0\rho_{m0}}\left\{\vec{k} \times \left(\vec{k} \times \left[\hat{\vec{U}} \times \vec{B}_0\right]\right)\right\} \times \vec{B}_0 + V_s^2\vec{k}(\vec{k} \cdot \hat{\vec{U}}) \tag{6.41}$$

Without loss of generality we can assume that $\vec{B}_0 = (0, 0, B_0)$ and that $\vec{k} = (k\sin(\theta), 0, k\cos(\theta))$ as figure 6.1 shows

By doing the cross products of the equation 6.41, dividing by k^2 and factoring by B_0^2:

$$\left(\frac{\omega}{k}\right)^2 \begin{bmatrix} \hat{U}_x \\ \hat{U}_y \\ \hat{U}_z \end{bmatrix} = V_A^2 \begin{bmatrix} \hat{U}_x \\ \hat{U}_y\cos^2\theta \\ 0 \end{bmatrix} + V_S^2 \begin{bmatrix} \hat{U}_x\sin^2\theta + \hat{U}_z\sin\theta\cos\theta \\ 0 \\ \hat{U}_x\sin\theta\cos\theta + \hat{U}_z\cos^2 \end{bmatrix}$$

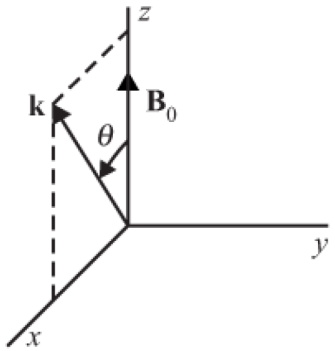

Figure 6.1: Coordinates for analyzing waves in MHD

Where $V_A = \dfrac{B_0}{\sqrt{\mu_o \rho_{m0}}}$ is known and is known as Alfvén velocity. Now, if $v_p = \omega/k$ is replaced by the phase velocity, this equation becomes:

$$\begin{bmatrix} v_p^2 - V_s^2 \sin^2\theta - V_A^2 & 0 & -V_s^2 \sin\theta\cos\theta \\ 0 & v_p^2 - V_A^2\cos^2\theta & 0 \\ -V_s^2 \sin\theta\cos\theta & 0 & v_p^2 - V_S^2\cos^2\theta \end{bmatrix} \begin{bmatrix} \hat{U}_x \\ \hat{U}_y \\ \hat{U}_z \end{bmatrix} = 0$$

Which has non-trivial solutions for $\hat{\vec{U}}$ only if the determinant of the matrix is 0. Therefore, the dispersion relation becomes:

$$D(k,w) = (v_p^2 - V_A^2\cos^2\theta)\left[v_p^4 - v_p^2(V_A^2 + V_S^2)^2 + V_A^2 V_S^2 \sin^2\theta\right] \tag{6.42}$$

In turn, this has three roots:

$$v_p^2 = 0.5(V_A^2 + V_S^2) - 0.5\sqrt{(V_A^2 - V_S^2)^2 + 4V_A^2 V_S^2 \sin^2\theta} \tag{6.43}$$

$$v_p^2 = V_A^2\cos^2\theta \tag{6.44}$$

$$v_p^2 = 0.5(V_A^2 + V_S^2) + 0.5\sqrt{(V_A^2 - V_S^2)^2 + 4V_A^2 V_S^2 \sin^2\theta} \tag{6.45}$$

These solutions are known as the slow magnetosonic mode, Alfvén mode and fast magnetosonic mode respectively.

6.2.1 Transverse Mode: Alfvén Mode

It is easy to prove that the root presented is indeed such. If the eigenvectors are obtained for the case:

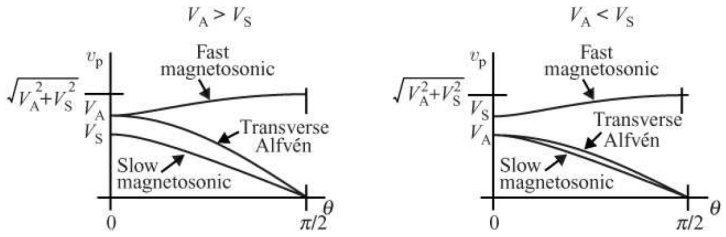

Figure 6.2: Phase velocity charts for analyzing waves in MHD

$$\hat{\vec{U}} = (0, \hat{U}_y, 0) \tag{6.46}$$

$$\hat{\vec{B}} = (0, \hat{B}_y, 0) \qquad \hat{B}_y = -B_0(\frac{\hat{U}_y}{V_a})Sing(\cos\theta) \tag{6.47}$$

$$\hat{\vec{E}} = (\hat{E}_X, 0, 0) \qquad \hat{E}_x = -B_0\hat{U}_y \tag{6.48}$$

$$\hat{\rho_m} = 0 \tag{6.49}$$

Thus, it can be seen that the movement of the fluid is completely transverse without compressional component ($\vec{k} \cdot \vec{U} = 0$). The speed of propagation is completely controlled by the speed of Alfvén. Also it is important to note that the poynting vector goes in a direction parallel to the static magnetic field $\vec{B}_0$ where $\vec{S} = (1/\mu_0)\hat{\vec{E}} \times \hat{\vec{B}}$. This is best represented in the figure 6.3.

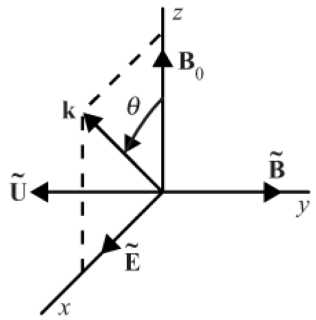

Figure 6.3: Eigenvectors for the case of Alfvén mode

In addition, from the relation obtained in 6.44 the group velocity can be extracted:

$$\vec{v}_g = \vec{\nabla}_{\vec{k}}\omega = V_a\hat{z} \tag{6.50}$$

Which ends up being parallel to the static magnetic field. This mode has an interesting analogy with a tense string fixed at its ends.

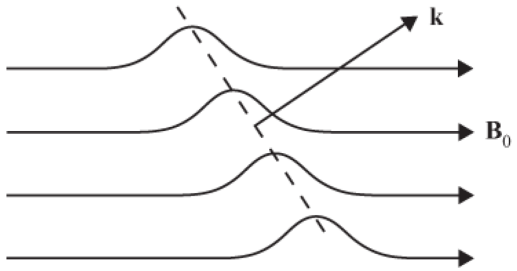

Figure 6.4: Mode propagation analogy for the Alfvén case

6.2.2 Fast and slow magnetosonic modes

Given the dispersion relations shown in 6.43 and 6.45, these modes depend on both the magnetic field (through Alfvén velocity) and plasma pressure (through the velocity of sound). Thus, for oblique propagation angles we have a velocity component parallel to $\vec{k}$. In contrast, the magnetosonic mode has both transverse and longitudinal components.

As an example, for angles $\theta = 0$ and $\theta = \pi/2$ the following homogeneous equations appear:

$$\begin{bmatrix} v_p^2 - V_A^2 & 0 \\ 0 & v_p^2 - V_S^2 \end{bmatrix} \begin{bmatrix} \hat{U}_x \\ \hat{U}_z \end{bmatrix} = 0$$

In this case the two roots are clearly seen, where $v_p^2 = V_A^2$ and $v_p^2 = V_S^2$. Thus, the difference between fast and slow mode comes from the differences between V_A and V_S. If $V_A > V_S$, $v_p^2 = V_A^2$ is the fast mode and $v_p^2 = V_S^2$ is the slow mode. In the opposite case the classification is reversed. When obtaining the eigenvectors,the following figure can be plotted:

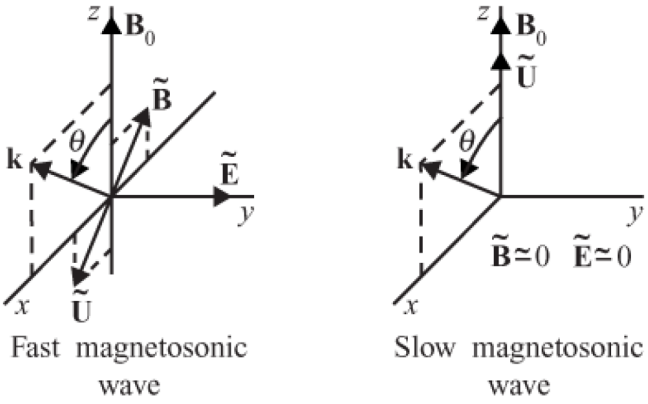

Figure 6.5: Eigenvectors for each mode of propagation

To put into perspective, V_A in the magnetosphere has a value of approximately 1000 km/s

Chapter 7

Appendix B: PC5 Drivers

7.1 Upstream Waves

One way of generating pulsations in the mid frequency range is given by the penetration to the magnetosphere by waves generated in the upstreaming SW (foreshock region) by protons reflected by the bowshock. These will be generated when it is true that:

$$|\omega - \vec{k} \cdot \vec{V_p}| = \Omega_p \tag{7.1}$$

Where ω is the wave frequency, $\vec{V_p}$ is the velocity of the reflected protons ($\approx 600 - 1200$ km / s) in the SW reference frame and Ω_p is their gyro-frequency. In the frame of reference of a satellite, this would be:

$$\omega_s = \omega + \vec{k} \cdot \vec{V}_{SW} \tag{7.2}$$

Assuming that these velocities are greater than the Alfvén velocity (which is true in the interplanetary medium) the dispersion relation in the case of the uniform mode $\omega = \vec{k} \cdot \vec{V_A}$ can be written:

$$\omega_s \approx \Omega_p \frac{V_{SW}}{V_p} \frac{\cos\theta_1}{\cos\theta_2} \tag{7.3}$$

Where θ_1 is the angle between $\vec{k}$ and $\vec{V}_{SW}$ and θ_2 is the angle between $\vec{k}$ and $\vec{V_p}$. This shows that the frequency depends on the interplanetary medium, SW, and the velocity of protons.

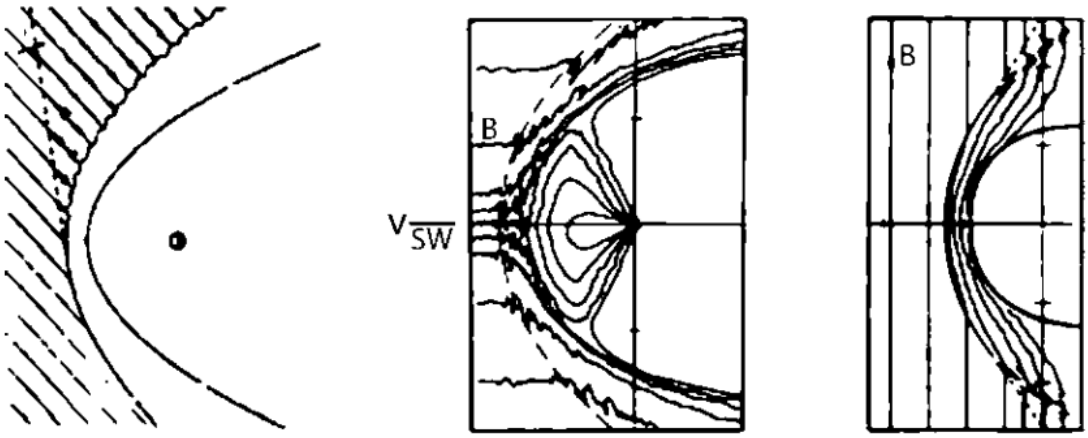

The foreshock region is located at the equator for the purpose of the figures. *Left panel* shows how the waves are generated along the IMF. *Central panel* shows that for the IMF radio components the waves are generated symmetrically in the foreshock region. *Right panel* shows that for a perpendicular IMF the waves are generated in small spaces close of the flanks of the bow shock

Figure 7.1: Generation by upstream waves and penetration of pulsations.

7.2 Kevin-Kelmholtz Instability (KHI)

Where n represents the density of particles and the suffixes SW and M are the solar wind and the magnetosphere respectively. Thus, KHI waves have a phase velocity in the same direction as the SW that generates them (to the west in the mornings and to the east at night).

$$(\vec{k}\cdot\vec{V}_{SW})^2 > (\frac{1}{n_{SW}}+\frac{1}{n_M})\times\left[n_{SW}(\vec{k}\cdot\vec{V}_A)^2_{sw}+n_M(\vec{k}\cdot\vec{V}_A)^2_M\right] \tag{7.4}$$

Where n represents the density of particles and the suffixes SW and M are the solar wind and the magnetosphere respectively. Thus, KHI waves have a phase velocity in the same direction as the SW that generates them (to the west in the mornings and to the east at night).

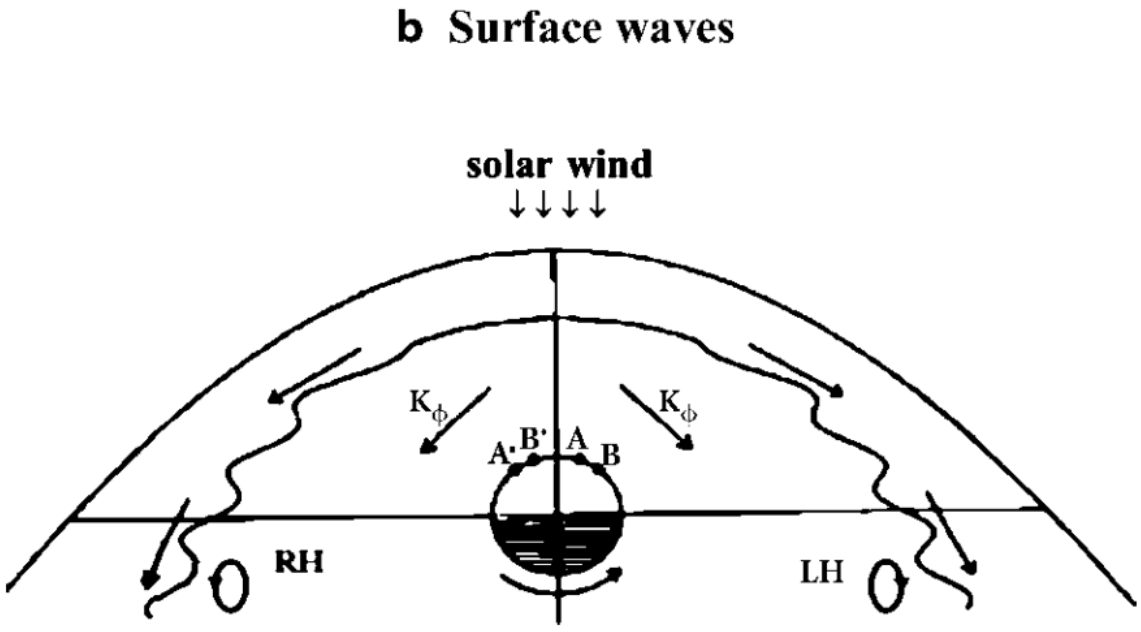

This image represents an outline of the generation and propagation of surface waves in the magnetopause. K_ϕ is the azimuthal component of the wave vector. A and B represents two different measuring stations. Since these waves propagate towards the tail, they should be reflected as a propagation from A to B when they are on the dawn side

Figure 7.2: Generation by KHI and penetration of pulsations.

7.3 Internal Amplifications

There are two processes by which the outer energy enters the magnetosphere. One is called field line resonance and the other cavity resonance. This again sees the field lines as tight strings, which can resonate both azimuthally and by changing the size of the cavity. In fact these two processes interact with each other.

7.3.1 Field Line Resonance

Field line resonance is the main mechanism and energy for ground pulsations. This can be seen with a simple model where the field lines in the magnetosphere are like an attenuated harmonic oscillator in the presence of a forcing. FLR occurs when the frequency of the incoming wave (driving) is comparable to the natural frequency of the field line. If the monochromatic wave is f^*, the coupling will be larger with a magnetic field line of frequency f^*. Thus, we can see that in equilibrium the field lines, or these tight strings, do not move. Given a process that takes them out of balance, a voltage is born to return to equilibrium, but it is known that these field lines are full of spinning particles that charge momentum, the system has a constant overshoot, so it remains oscillating. This phenomenon is explained in the figure 7.3.

In this process we can find the toroidal mode (and the poloidal to some extent). The

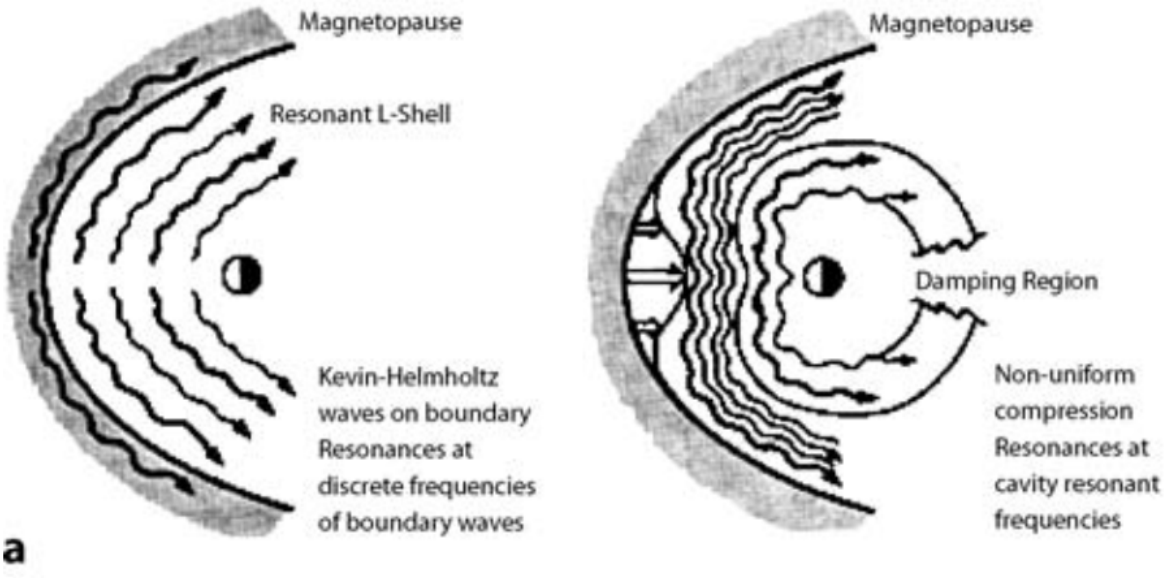

The difference between the waves generated by KHI in the magnetopause (left) and the cavity mode generated by the compression of the nose of the magnetopause is shown schematically. The thickness of the lines represents the magnitude of the field. By the same it is possible to be seen how for the case of KHI the amplitude decreases when approaching the earth but it has local excitations in the resonant lines. In this case the azimuthal component of the wave is amplified.

Figure 7.3: FLR schematic demonstration

toroidal mode most seen in space given that azimuthal perturbations do not change the magnitude of the field or changes in plasma density. In addition, nearby lines generally have the same natural frequency, so they may be in phase with the initial disturbance.